# Supporting information

## Substrate-dependent Spin Crossover in a Fe(II) scorpionate complex.

Margaux Pénicaud,[a] Edoardo Martinez,[b] Giulia Serrano,[b,c] Brunetto Cortigiani,[b] Lorenzo Squillantini,[b] Juan H. González-Estefan,[a] Emilio Velez-Fort,[d] Mathieu Duttine,[a] Mathieu Gonidec,[a] Patrick Rosa,*[a] Matteo Mannini,[b] Lorenzo Poggini,*[b,e]

[a] *Univ. Bordeaux, CNRS, Bordeaux-INP, ICMCB, UMR 5026, F-33600 Pessac, Cedex.*
[b] *Department of Chemistry "U. Schiff" (DICUS) and INSTM Research Unit, University of Florence, Via della Lastruccia 3-13, 50019 Sesto Fiorentino (FI), Italy.*
[c] *Department of Industrial Engineering (DIEF) and INSTM Research Unit, University of Florence, Via di Santa Marta, 3, 50139, Florence, Italy.*
[d] *European Synchrotron Radiation Facility, 71, avenue des Martyrs CS 40220, 38043 Grenoble Cedex 9, France.*
[e] *Institute for Chemistry of OrganoMetallic Compounds (ICCOM-CNR), Via Madonna del Piano, 50019 Sesto Fiorentino (FI), Italy.*
Electronic Supplementary Information (ESI) available: [details of any supplementary information available should be included here]. See DOI: 10.1039/x0xx00000x

### Experimental Section

Potassium borohydride (≥ 98%) was received from TCI chemicals. 1-*H*-pyrazole (≥ 98%); Iron(II) tetrafluoroborate hexahydrate (≥ 97%) and Iron(II) perchlorate hydrate (≥ 98%) were received from Aldrich. 3,5-dimethyl-1-*H*-pyrazole (≥ 99%) was received from Fluka. Iron(II) sulfate heptahydrate (≥ 99%) was received from Alfa Aesar. Toluene (≥ 99.3%) was received from Sigma-Aldrich. Heptane (≥ 99%) and methanol (≥ 99.9%) were received from Scharlab. Hexadecane (≥ 99%) and diethyl ether (≥ 99.7%) were received from S.D.S. Diethyl ether was dried over KOH, and methanol was distilled over magnesium prior to use. Complexation with the iron(II) salt was performed under argon atmosphere using standard Schlenk techniques.

### Preparation of the heteroscorpionate salt $KHB(pz)_2(dmpz)$

Synthesis of the title compound was attempted following three different procedures, the classical neat thermolytic reaction (A), a one-pot reaction in solution (B) and metathetic exchange of azoles (C). Path C proved to be unfruitful. Both paths A and B led to a mixture of tri-substituted borohydrides ($HBR_3$) containing different ratios of 1*H*-pyrazole (pz) and 3,5-dimethyl-1*H*-pyrazole (dmpz), as expected from reports on similar heteroscorpionate systems

found in the literature. From path A, the target ligand is mostly an impurity in $KHB(pz)_3$ (**Figure S2**). From path B, it can be obtained as the majority product in the mixture (**Figure S3**) thanks to a simple but crucial washing step. ESI-MS analysis on the crude B product before washing are given in **Figure S4** for comparison. Prior to the purification step, the homoscorpionate ligand $KHB(pz)_3$ is the main product, as with path A. However, one can notice that the amount of target ligand $KHB(pz)_2(dmpz)$ relative to $KHB(pz)_3$ is qualitatively much higher in batch B compared to A (75.2% from B and 13.7% from A). Thus, reaction path B may be preferred over the classical thermolytic synthesis, as it requires only one step and gives higher yields.

### Path A: Multistep synthesis of $KHB(pz)_2(dmpz)$ (A1, A2)

**Step 1**, synthesis of $KH_2B(pz)_2$ (**A1**): $KBH_4$ (8.64 g, 0.16 mol) and 1-*H*-pyrazole (27.935 g, 0.41 mol) were mixed in a round bottom flask fitted with a Vigreux column and connected to a volume meter. The mixture was heated to 105 °C and vigorous stirring started after the pyrazole has melted (~75° C). After 24h, 7.74 L of $H_2$ (0.316 mol) had evolved from the reaction. Heating was stopped and 20 mL of toluene were added in the mixture to prevent aggregation. Once cooled, the product was collected by filtration. The white powder was washed with 2x 30 mL of warm toluene to remove any unreacted pyrazole and dried in air, giving 23.96 g of $KH_2B(pz)_2$ (80% yield). **Elemental analysis** calculated for $C_6H_8BKN_4$ (186.06 $gmol^{-1}$): C 38.73%, N 30.11%, H 4.33%, B 5.81%, K 21.01%. Found: C 38.4(6)%, N 27.1(1)%, H 4.86(8)%, B 10.18%, K 18.56%. **$^1$H NMR** (400MHz, $D_2O$): 7.68 (2H), 7.56 (2H), 6.26 (2H), see spectrum **Figure S1**. **ATR-IR** spectrum showed the expected $BH_2$ multiplet around 2270-2430 $cm^{-1}$. For more details report to the spectra **Figure S8** and corresponding list of peaks in **Table S1**. **ESI-ITMS**(-) (MeOH), m/z (%) M=$C_6H_8BN_4^-$ : [2M+$K^+$] calculated 333.13 ; observed 332.92 (100) ; [M] calculated 147.08 ; observed 147.18 (76.1) ; [3M+2$K^+$] calculated 519.18 ; observed 518.49 (26.3) ; [2M+$Na^+$] calculated 317.16 ;

observed 317.23 (8.7) ; [M-$C_3H_5BN_2$ = $pz^-$] calculated 67.03 ; observed 66.89 (5.6) ; [3M+$Na^+$+$K^+$] calculated 503.21 ; observed 502.64 (3.3). Isotopic distribution around observed peaks matches with theoretical predictions.

**Step 2**, synthesis of $KHB(pz)_2(dmpz)$ (**A2**): $KH_2B(pz)_2$ **A1** (3.719 g, 20 mmol) and 3,5-dimethyl-1*H*-pyrazole (2.357 g, 24 mmol) were mixed in a round bottom flask fitted with a Vigreux column and connected to a volume meter. The mixture was heated to 155 °C and vigorous stirring started after melting of the dimethylpyrazole (~100° C). After 15h, 0.41 L of $H_2$ (16.7 mmol) had evolved from the reaction (~83% yield). Heating was stopped and the product was suspended in 75 mL of diethyl ether. Solid residues were filtered off, and the diethyl ether was removed using a rotary evaporator. After further drying under vacuum, the product was obtained as a translucent viscous oil (4.328 g). Unreacted dimethylpyrazole was removed by sublimation on a cold finger under vacuum (heating at ~70 °C and cooling the finger with water at 0 °C). Due to the high viscosity of the product, non-negligible amounts could be easily lost when transferring from the reaction flask to other containers. Any attempts of drying or crystallisation were unsuccessful. Mass Spectrometry (MS) showed that the product was a mixture containing $KHB(pz)_3$ as the main product, and the target ligand $KHB(pz)_2(dmpz)$ as a side product (see **Figure S2**). **Elemental analysis** calculated for $C_{11}H_{14}BKN_6$ (280.18 $gmol^{-1}$): C 47.16%, N 29.99%, H 5.04%. Found: C 39.14(9)%, N 23.67(17)%, H 5.71(6)%. **ATR-IR** spectrum: see **Figure S9** and corresponding list of peaks in **Table S1**.

### Path B: One-pot synthesis of $KHB(pz)_2(dmpz)$ (B1)

$KBH_4$ (1.069 g, 19.8 mmol), 1*H*-pyrazole (2.722 g, 40 mmol) and 3,5-dimethyl-1*H*-pyrazole (1.924 g, 20 mmol) hexadecane were suspended in 60 mL of in a 250 mL round-bottom flask. The flask was equipped with a Vigreux column connected to an argon line and a volume meter. The experimental setup was purged under a flow of argon for 30 min prior to the reaction. The

reaction mixture was heated from room temperature to 278 °C over the course of 4 hours, with constant stirring. At this point, the theoretical amount of hydrogen (1.47 L, 60 mmol) had evolved from the reaction. The heating was continued for 30 minutes, then the reaction mixture was allowed to cool down to 100 °C. 100 mL of heptane were added and the mixture was left to stand at rt overnight. Upon cooling the product formed a compact white mass at the bottom of the reaction flask and was impossible to recover. The solvents were then removed, and the solid rinsed with 3x20 mL of heptane. 60 mL of toluene was poured onto the solid and the product left to dissolve for 4 days. The resulting suspension was filtered and the toluene removed under reduced pressure. The crude product was obtained as a white viscous solid. It was then suspended in 81 mL of $Et_2O$ and filtered to obtain a white powder. MS shows that the product is a mixture containing both $KHB(pz)_2(dmpz)$ as the main product, and $KHB(pz)_3$ as a side product (see **Figure S3**). **Elemental analysis** calculated for $C_{11}H_{14}BKN_6$ (280.18 $gmol^{-1}$): C 47.16%, N 29.99%, H 5.04%. Found: C 47.6(2.4)%, N 24.5(5)%, H 6.13(7)%. **ATR-IR** spectrum showed the expected BH singlet peak at 2446 $cm^{-1}$. For more details see **Figure S10** and corresponding list of peaks in **Table S1**.

### Path C: High-temperature metathesis (C1)

KTp* (1.682 g, 5 mmol) and 1*H*-pyrazole (0.681 g, 10 mmol) were suspended in 15 mL of hexadecane in a 100 mL flask. The flask was fitted with a Vigreux column connected to an argon line. The solvent and the entire experimental assembly were purged by bubbling under argon flow before the reaction. The mixture was heated under agitation to 252°C to observe a slight reflux of the solvent. The temperature was maintained for a total of 4h (including 1h temperature rise) then the mixture was left to cool. When reaching 100°C, the formation of a white powder was observed in the flask. 25 mL of heptane were added and the reaction was stirred for 2 hours before filtering. The solution was then concentrated by natural evaporation until a new solid phase was obtained, which was recovered by filtration and rinsed with 2x 20

mL of heptane, then 2x 10 mL of petroleum ether. After drying, 771.6 mg of white-yellow powder with a heterogeneous appearance (**C1**) is obtained. Mass spectrometry analysis of the crude product showed that it consisted of a mixture of tetrasubstituted ligands ($pzTp^-$, $Bpz_3dmpz^-$, $Bpz_2dmpz_2^-$ and $pzTp^{*-}$), detected alone and in the form of dimers or trimers associated with potassium (**Figure S5**). It is noteworthy that those ligands have not been reported to the best of our knowledge, but their separation and purification is out of the scope of this work. Since their formation was favoured by the high temperature used, we checked the same reaction in the same temperature conditions than path A.

**Path C: Low-temperature metathesis (C2)**

KTp* (200.3 mg, 0.6 mmol) and 1*H*-pyrazole (80.9 mg, 1.2 mmol) were suspended in 2 mL of hexadecane in a 50 mL flask. The flask was fitted with a Vigreux column connected to an argon line. The solvent and the entire experimental assembly were purged by bubbling under argon flow before the reaction. The mixture was stirred then heated up to 150°C, and this temperature was maintained for 4 hours. After cooling down, 10 mL of heptane were added and the solution was stirred overnight. A solid in suspension was observed, and recovered by filtration on a nylon membrane, then rinsed with 20 mL of petroleum ether. The raw product was a beige pasty solid (C2) which was analyzed by mass spectrometry. The signals obtained indicated that the product is a mixture, but their formal identification could not be achieved. However, it should be noted that none of the peaks is compatible with a bis-, tris- or tetra-substituted scorpionate by pz, dmpz or a mixture of these species. The isotopic distribution of the signals could correspond to species containing an increasing number of boron atoms, with two B atoms for the lighter fragment. Pyrazabole species [1,2] or some kind of coordination

[1] Trofimenko, S. *J. Am. Chem. Soc.* **89**, 3165–3170 (1967).
[2] rock, C. P., Niedenzu, K., Hanecker, E. & Nöth, H. *Acta Crystallogr. Sect. C Cryst. Struct. Commun.* **41**, 1458–1463 (1985).

polymer could have been formed, with peaks separated by the loss of a fragment of 173-174 Da that could be HB(pz)(dmpz).

### Preparation of the heteroscorpionate Fe(II) complex [Fe(HB(pz)$_2$(dmpz))$_2$] 1

From the diethylether washed ligand B, we were able to prepare pure complex **1** using classical liquid-liquid slow-diffusion techniques, with subsequent manual triage and sublimation. While by using the crude ligand B for the complexation, as often done in the literature, we obtained product **1'**. Elemental analysis on **1'** gives a value matching with [Fe(HB(pz)$_2$dmpz)$_2$] contaminated with a significant fraction (20%) of [Fe(HB(pz)$_3$)$_2$], or their corresponding heteroleptic complex. However, MS revealed that **1'** is a mixture of possibly nine complexes with composition ranging from [Fe(HB(pz)$_3$)$_2$] to [Fe(HB(pz)(dmpz)$_2$)(HB(dmpz)$_3$)] (**Figure S7**). **Elemental analysis** on **1'** calculated for $C_{22}H_{28}B_2FeN_{12}$-($C_{18}H_{20}B_2FeN_{12}$)$_{0.2}$ (634.39 gmol$^{-1}$): C: 48.45%, N: 31.81%, H: 5.08%, found C: 48.27(5)%, N: 31.7(1)%, H: 5.254(4)%

**Synthesis of [Fe(HB(pz)$_2$(dmpz))$_2$] (1)**: The Fe(II) complex was prepared by slow diffusion crystallization in freshly distilled methanol. In two separated Schlenk tubes were weighed 90.8 mg (0.325 mmol) of $FeSO_4.7H_2O$ and 182.9 mg (0.65 mmol) of the **B1** ligand. The products were placed under argon atmosphere, and dissolved in 3 mL of freshly distilled methanol. A buffer layer (4 mL of pure methanol) was slowly added on top of the iron solution, then the ligand solution was slowly added on top of this separation layer, with care taken to disturb the least possible the iron precursor solution. The solutions were allowed to diffuse for five days, after which the solution was removed and the product dried under reduced pressure. In order to separate the compound from the potassium salts that precipitate during the diffusion, the reaction products were suspended in ethanol and filtered, then washed with small amounts of water until the liquid phase remains colourless. It was then rinsed with ethanol and dried in air. The complex was obtained as dark violet microcrystals (37.6 mg, 21% yield). The same

preparation was performed starting from various iron(II) precursor salts ($FeSO_4 \cdot 7\,H_2O$ ; $Fe(BF_4)_2 \cdot 6\,H_2O$ et $Fe(ClO_4)_2 \cdot x\,H_2O$), yielding crystals of variable dimensions and quality (**Figure S11**), which were clearly mixed with some residual salt despite the washing. Nevertheless, mass spectra were similar for the three batches and showed the presence of the targeted complex (**Figure S6**), with a very minor impurity consisting of $[Fe(HBpz_3)(HBpz_2dmpz)]$. The crystals were isolated from the inorganic salts by careful manual triage under a microscope. Powder X-ray diffraction patterns acquired on the three batches showed very similar diffractograms (**Figure S12**, **Figure S13** and **Figure S14**). Satisfying Le Bail profile matching fits could be performed for all three batches to the same triclinic unit cell (**Table S2**), which corresponds nicely to the unit cell determined on a single crystal of complex **1** at 300 K (**Table S3**). Accordingly, the three batches were mixed together, yielding a total of 135.4 mg, and further purified by sublimation at *ca.* 140 °C under vacuum ($4.9e^{-6}$ mbar) onto a cold finger. Three batches were collected over three days. Similar mass spectra to the starting materials were obtained for the three batches (**Figure S6**). Powder diffraction patterns, though showing a degraded crystalline quality (**Figure S15**), could still be fitted to units cells (**Table S2**) congruent with the one measured at 300 K on a single crystal (**Table S3**). **Elemental analysis** calculated for $C_{22}H_{28}B_2FeN_{12}$ (538.01 $gmol^{-1}$): C 49.11%, N 31.24%, H 5.25%, B 4.02%, Fe 10.38%. Found: C 48.6(1)%, N 31.81(6)%, H 5.18(8)%, B 3.72%, Fe 9.71%. **MS** for $C_{22}H_{28}B_2FeN_{12}$ m/z: 538.21, found 538.33. Details on the spectrum are shown below (**Figure S6**).

**Nuclear Magnetic Resonance**

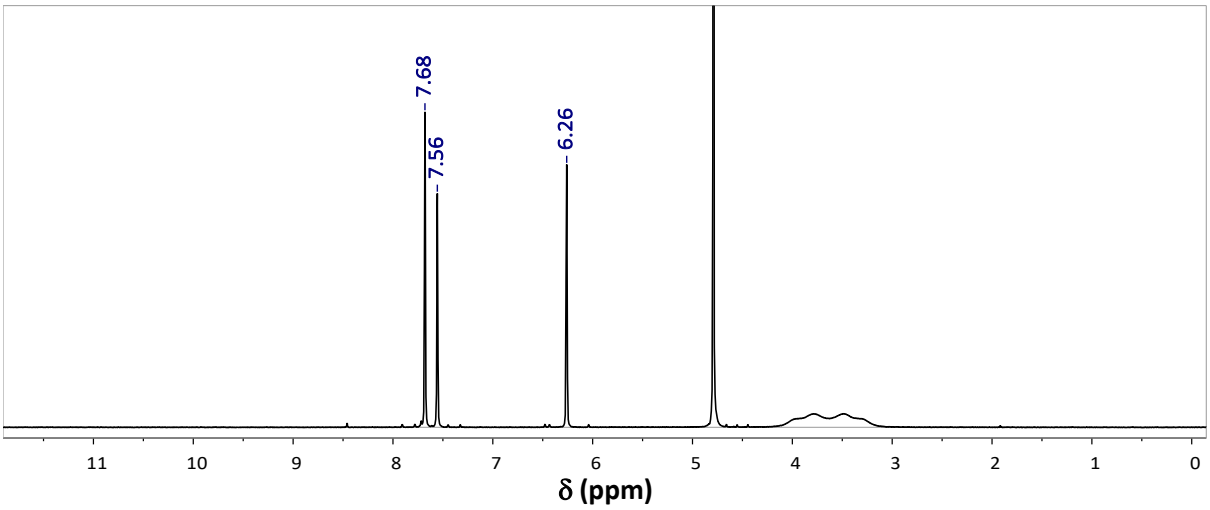


**Figure S1**: $^{1}H$ NMR of A1 in $D_2O$ recorded at 400MHz. The solvent peak is calibrated at 4.790 ppm. The peaks are consistent with what is reported by W. H. McCurdy, (*Inorg. Chem.*, **1975**, *14*, 2292–2294.)

**Mass spectrometry (Electro-Spray Ionization)**

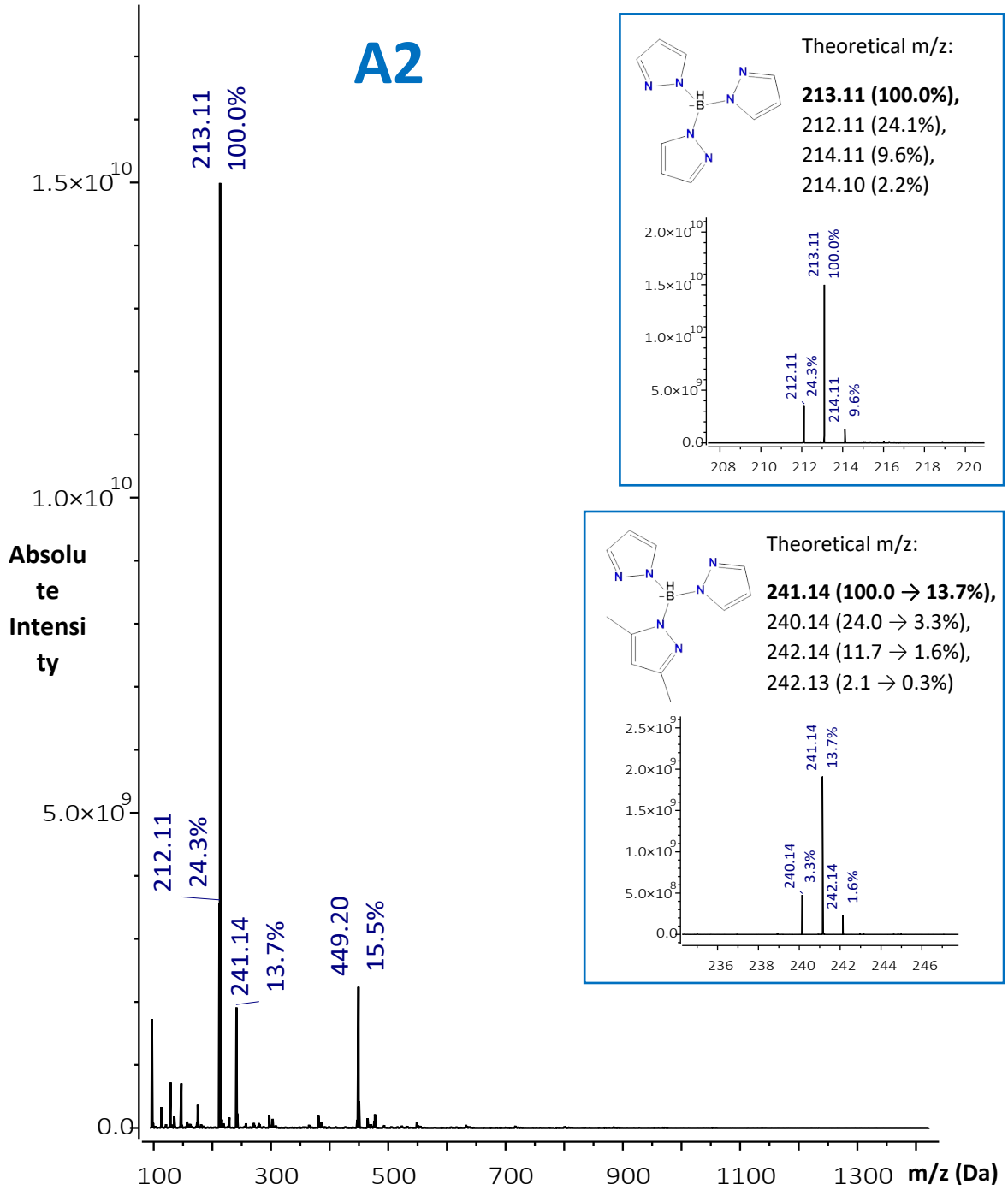


**Figure S2** ESI-MS of the ligand batch **A2** in negative polarization. The first peak on the left (m/z = 96.67) corresponds to 3,5-dimethypyrazole. Inserts show a magnification of the two main peaks with a drawing of their corresponding anionic ligand and theoretical isotopic distribution of the peak. The peak at m/z = 449.20 Da corresponds to $[(HB(pz)_3^-)_2;Na^+]$.

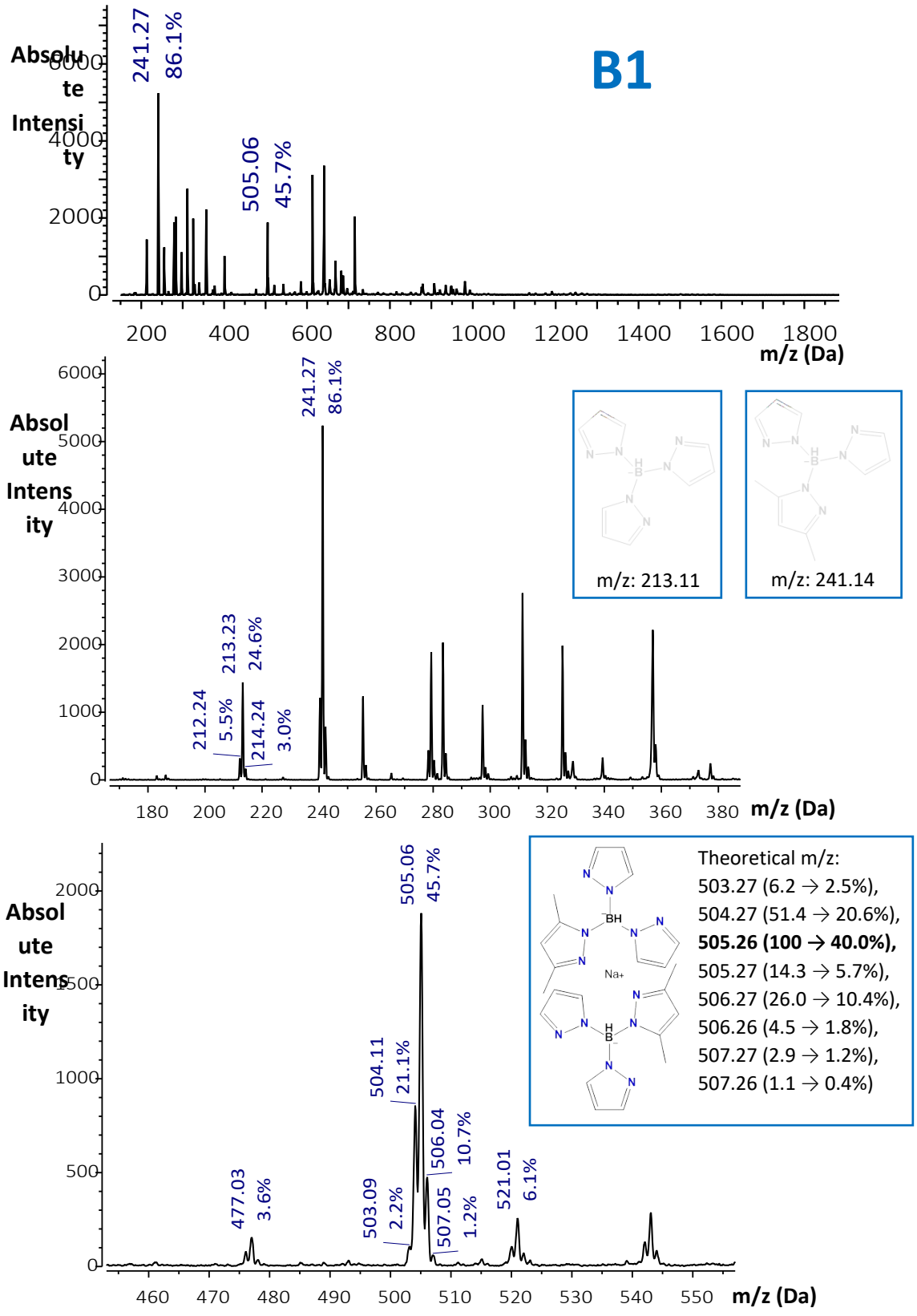


**Figure S3** ESI-MS of the ligand batch **B1** in negative polarization. Top: whole spectra. Middle: ligands molecular peaks and drawing of the corresponding anions. Bottom: zoom on

the peaks corresponding to pairs of ligands with a cation: $[Na(HBpz_3)(HBpz_2dmpz)]^-$ m/z = 477.23 Da, $[Na(HBpz_2dmpz)_2]^-$ see insert; $[K(HBpz_2dmpz)_2]^-$ m/z = 521.24 Da.

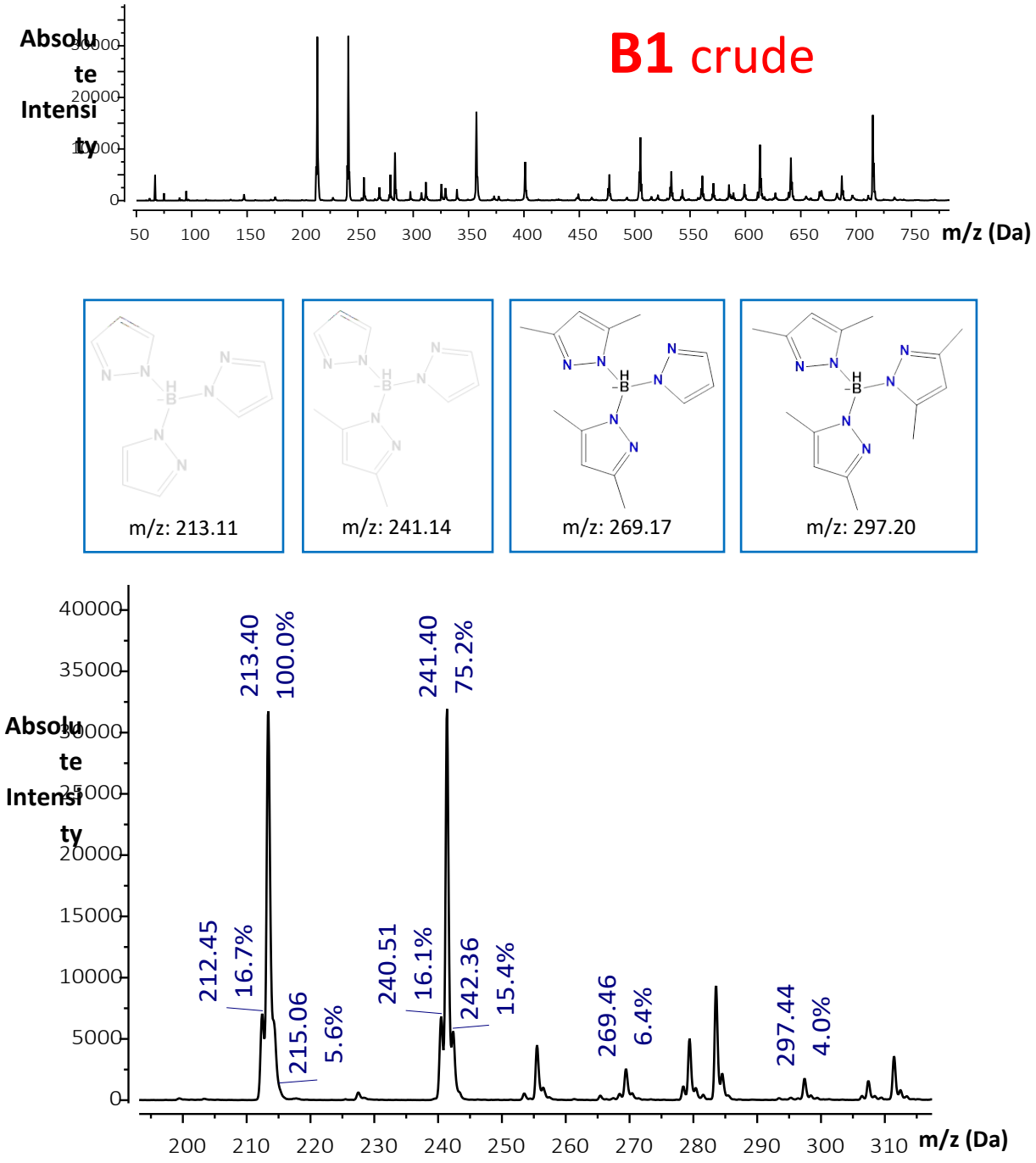


**Figure S4** ESI-MS of the ligand batch **B1** before washing with diethyl ether, in negative polarization. Top: overview of the whole spectrum. Bottom: Magnification of the spectra in the 195-315 Da region. Labelled peaks correspond to the four different combinations of poly-pyrazolyl borohydrides that can be obtained from pyrazole and 3,5-dimethylpyrazole, as drawn in the middle inserts.

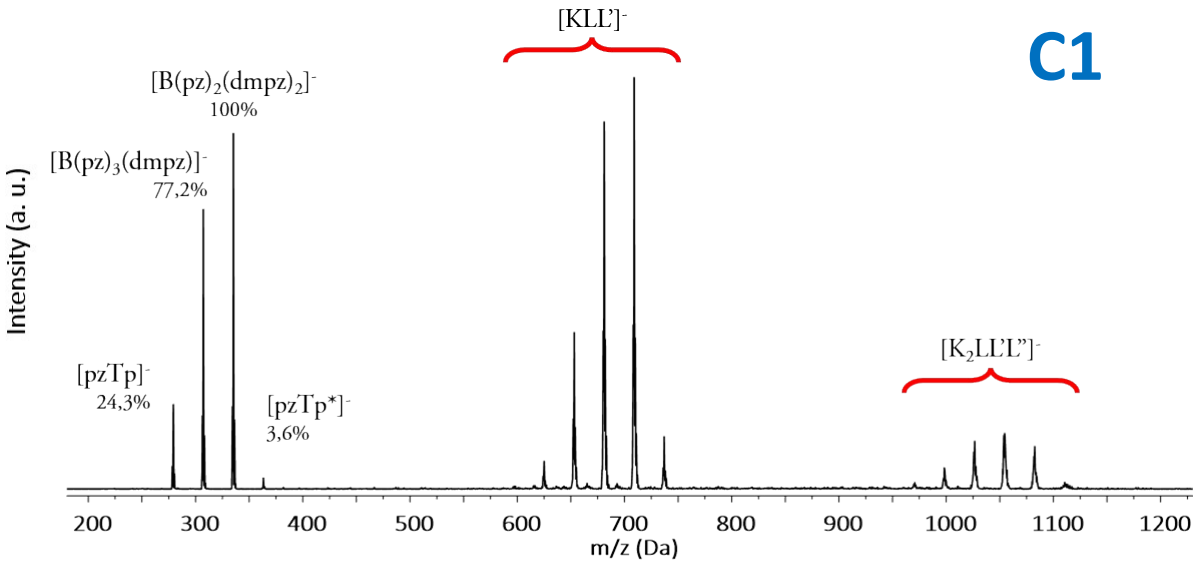


**Figure S5** ESI-MS of the ligand batch **C1**, in negative polarization. The product contains a mixture of tetrasubstituted ligands which are detected as isolated species or as clusters with potassium.

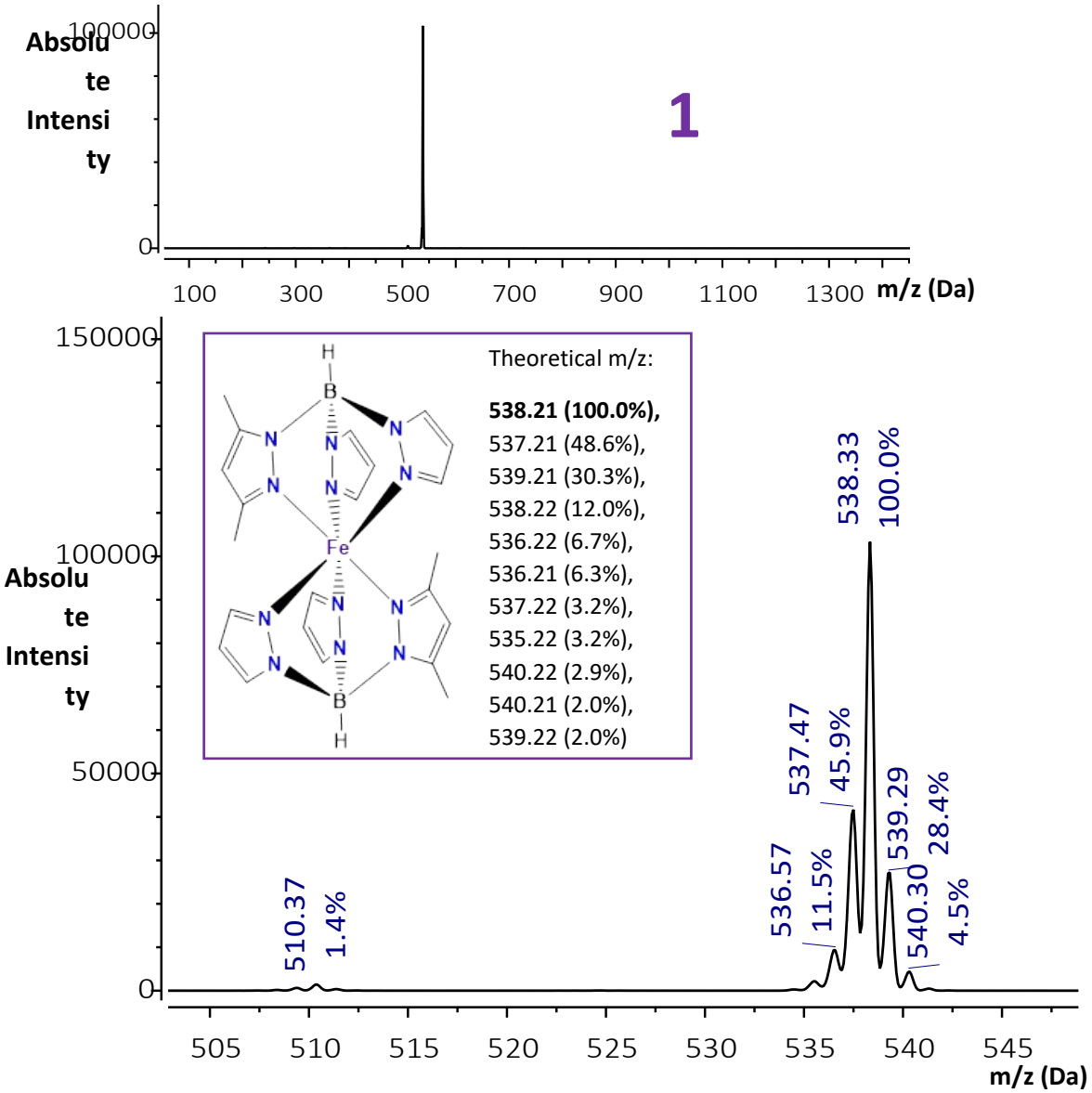


**Figure S6** ESI-MS of complex **1** (positive polarization). Top: view of the whole spectrum. Bottom: magnification on the peaks. The main one corresponds to complex **1**. Insert shows a drawing of the molecular structure and the predicted isotopic distribution of the peak. The peak at 510 Da corresponds to the heteroleptic complex [Fe(HBpz$_3$)(HBpz$_2$dmpz)].

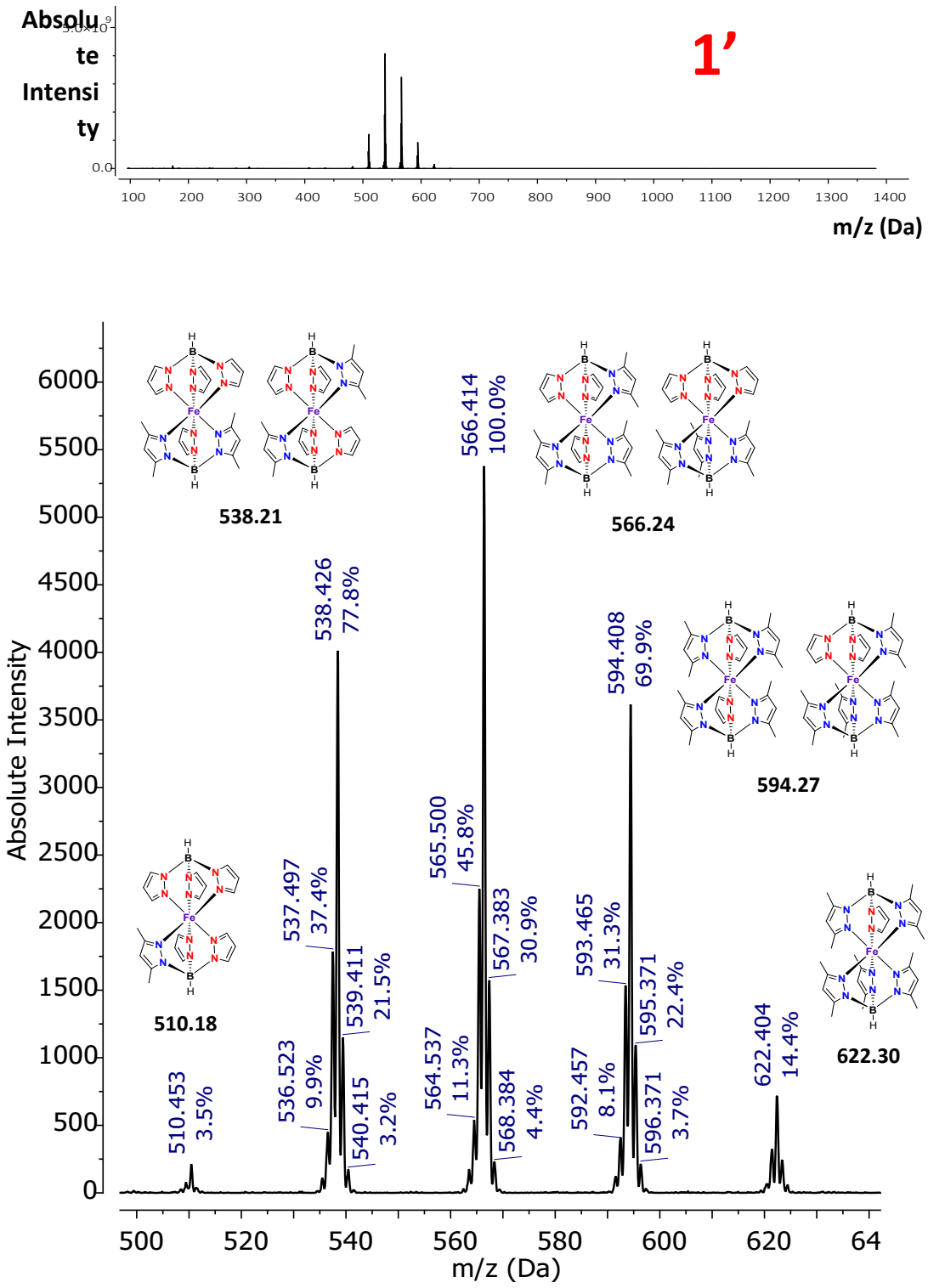


**Figure S7** ESI-MS (positive polarization) of product **1'** prepared from crude **B1** and purified by sublimation on a cold finger. Top: whole spectrum. Bottom: detailed view of the peaks and drawings of the possible complexes, with pz highlighted in red, dmpz in blue, and the mass of their predicted main isotopic peak.

**Attenuated Total Reflectance Infrared Spectroscopy**

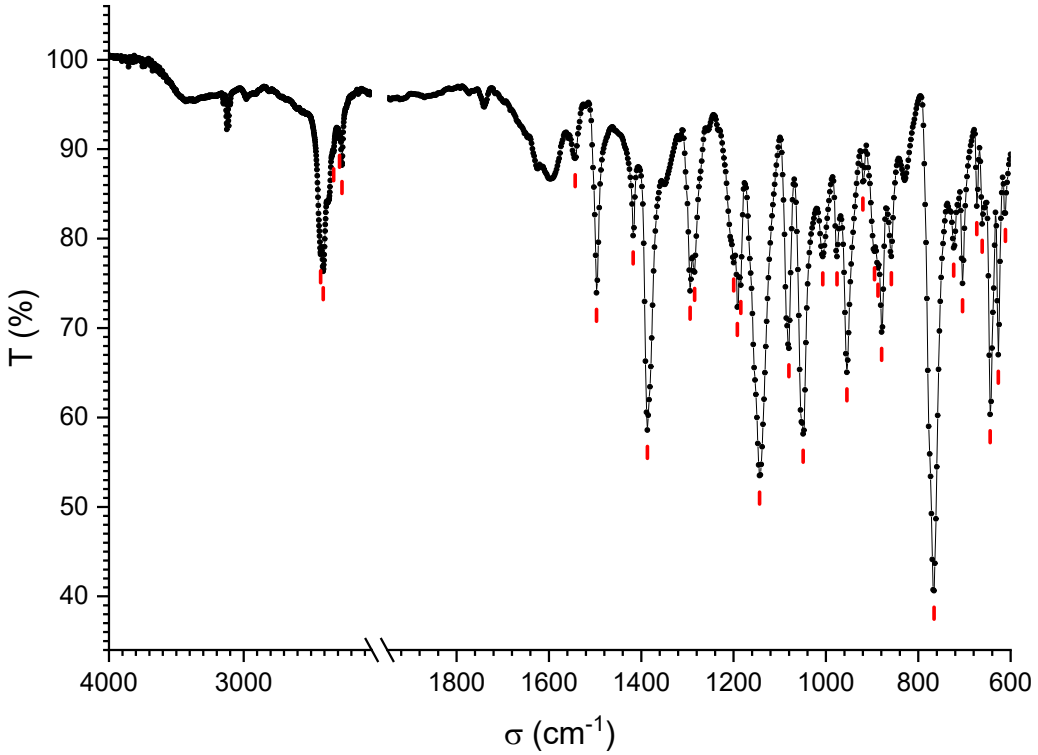


**Figure S8** ATR-IR spectra of compound **A1.** Red marks indicate the peaks listed in Table S1.

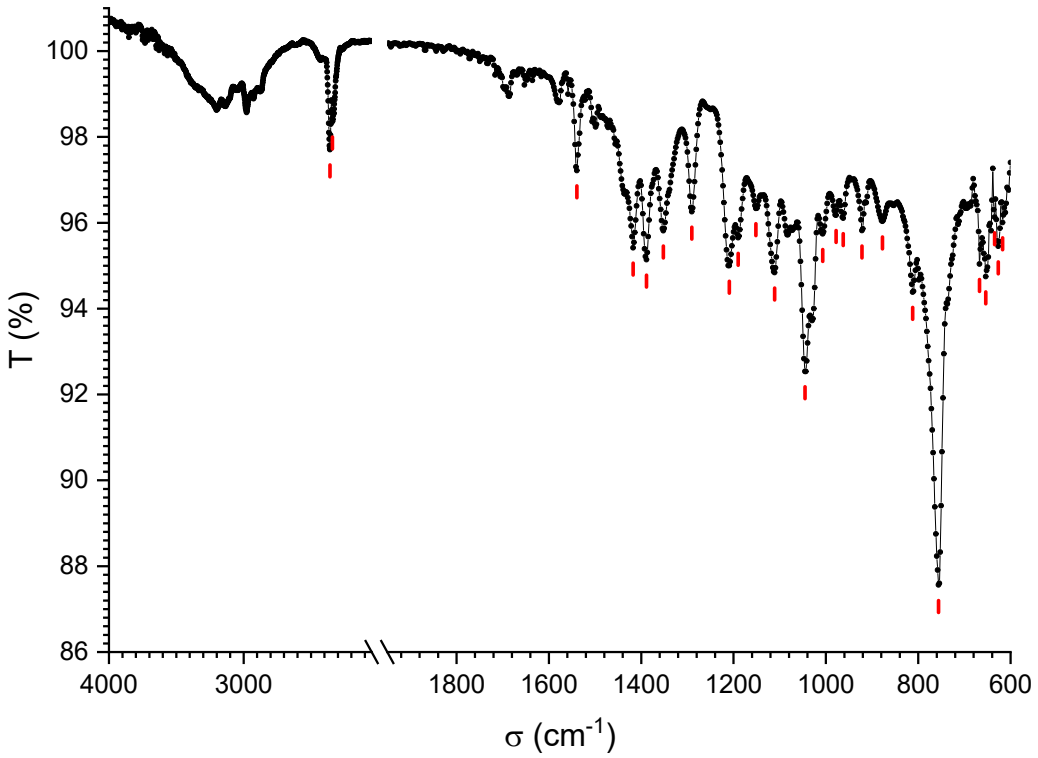


**Figure S9** ATR-IR spectra of compound **A2**. Red marks indicate the peaks listed in Table S1.

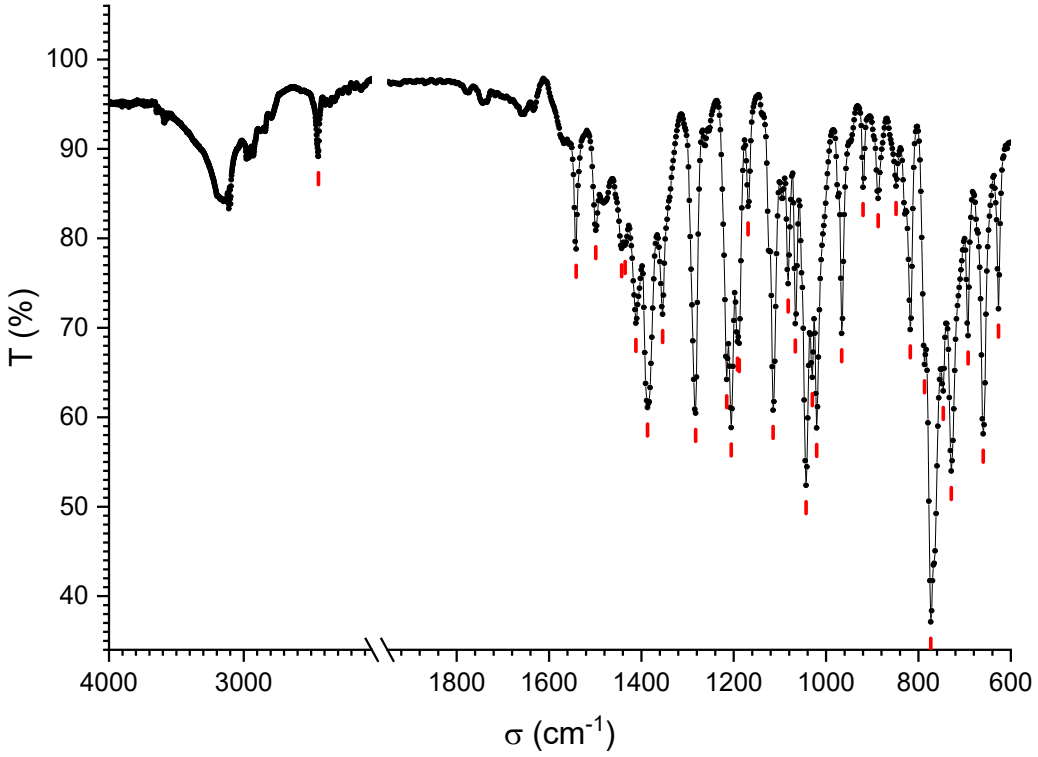


**Figure S10** ATR-IR spectra of compound **B1**. Red marks indicate the peaks listed in Table S1.

| Compound | A1 | A2 | B1 |
|---|---|---|---|
| Peaks ($cm^{-1}$) | 611.43 | 617.22 | |
| | 626.87 | 626.87 | 626.87 |
| | 644.22 | 634.58 | |
| | 661.58 | 653.87 | 659.66 |
| | 673.16 | 667.37 | |
| | 704.02 | | 692.44 |
| | 723.31 | | 729.09 |
| | | 756.1 | 746.45 |
| | 765.74 | | 773.46 |
| | | | 786.96 |
| | | 812.03 | 817.82 |
| | 858.32 | | 848.68 |
| | 879.54 | 877.61 | |
| | 887.26 | | 887.26 |
| | 894.97 | | |
| | 920.05 | 921.97 | 920.05 |
| | 954.76 | 962.48 | 966.34 |
| | 975.98 | 977.91 | |
| | 1006.84 | 1006.84 | |
| | | | 1020.34 |
| | | | 1029.99 |
| | 1049.28 | 1045.42 | 1043.49 |
| | | | 1066.64 |
| | 1080.14 | | 1082.07 |
| | | 1111 | 1114.86 |
| | 1143.79 | 1151.5 | 1168.86 |
| | 1184.29 | 1190.08 | 1188.15 |
| | 1192.01 | | 1192.01 |
| | 1199.72 | 1209.37 | 1205.51 |
| | | | 1215.15 |
| | 1284.59 | 1290.38 | 1282.66 |
| | 1294.24 | | |
| | | 1352.1 | 1354.03 |
| | 1386.82 | 1388.75 | 1386.82 |
| | 1417.68 | 1417.68 | 1411.89 |
| | | | 1435.04 |
| | | | 1442.75 |
| | 1496.76 | | 1498.69 |
| | 1543.05 | 1539.2 | 1541.12 |
| | 2270.22 | | |
| | 2287.58 | | |
| | 2331.94 | 2341.58 | |
| | | 2358.94 | |
| | 2409.09 | | 2445.74 |

**Table S1**: List of observed peaks from ATR-IR spectra of ligands A1, A2 and B1.

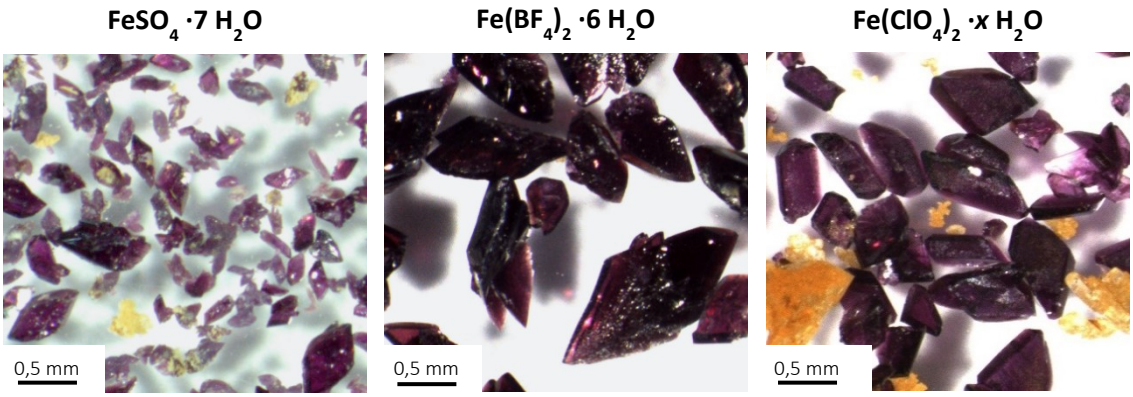


**Figure S11** Optical microscope pictures of [Fe(HB(pz)$_2$(dmpz))$_2$] crystals obtained from the various Fe(II) precursors.

**Crystallographic data**

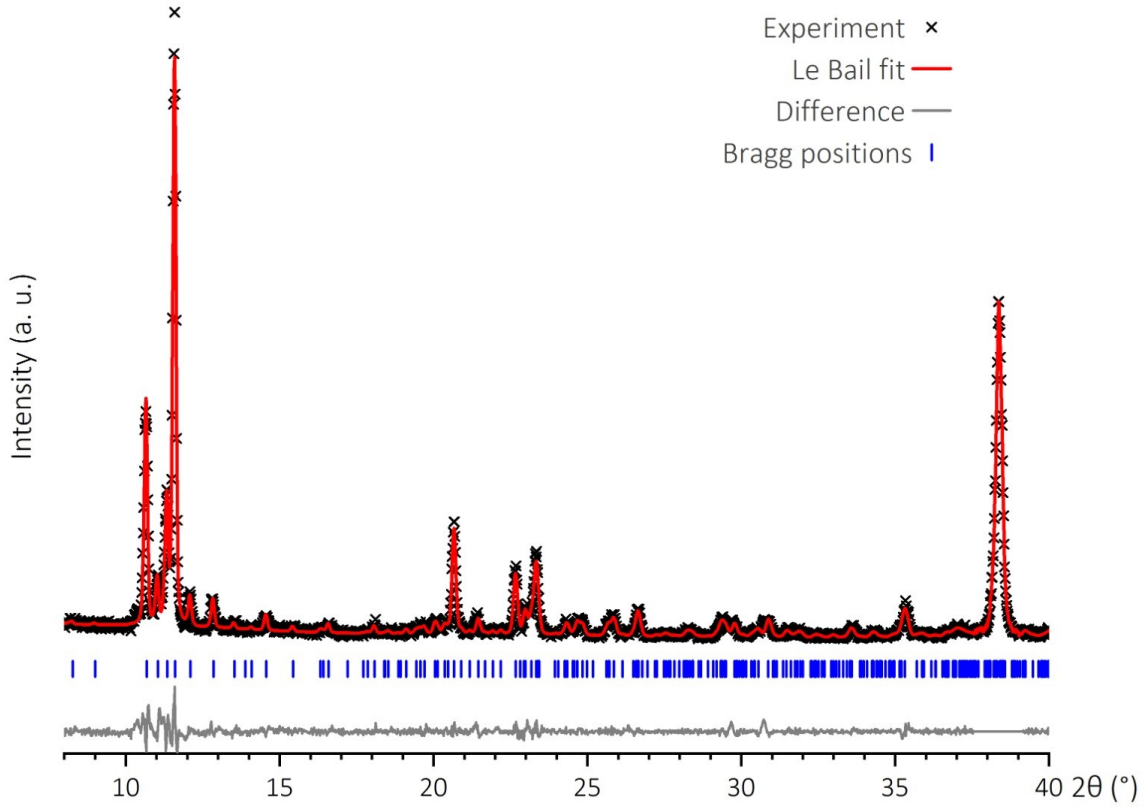


**Figure S12** Experimental powder diffraction pattern (black crosses) for complex **1** synthesized from $FeSO_4 \cdot 7\ H_2O$, Le Bail profile matching fit with parameters reported in **Table S2** (red lines), with corresponding Bragg peaks' positions (blue markers), and fit residual (grey line).

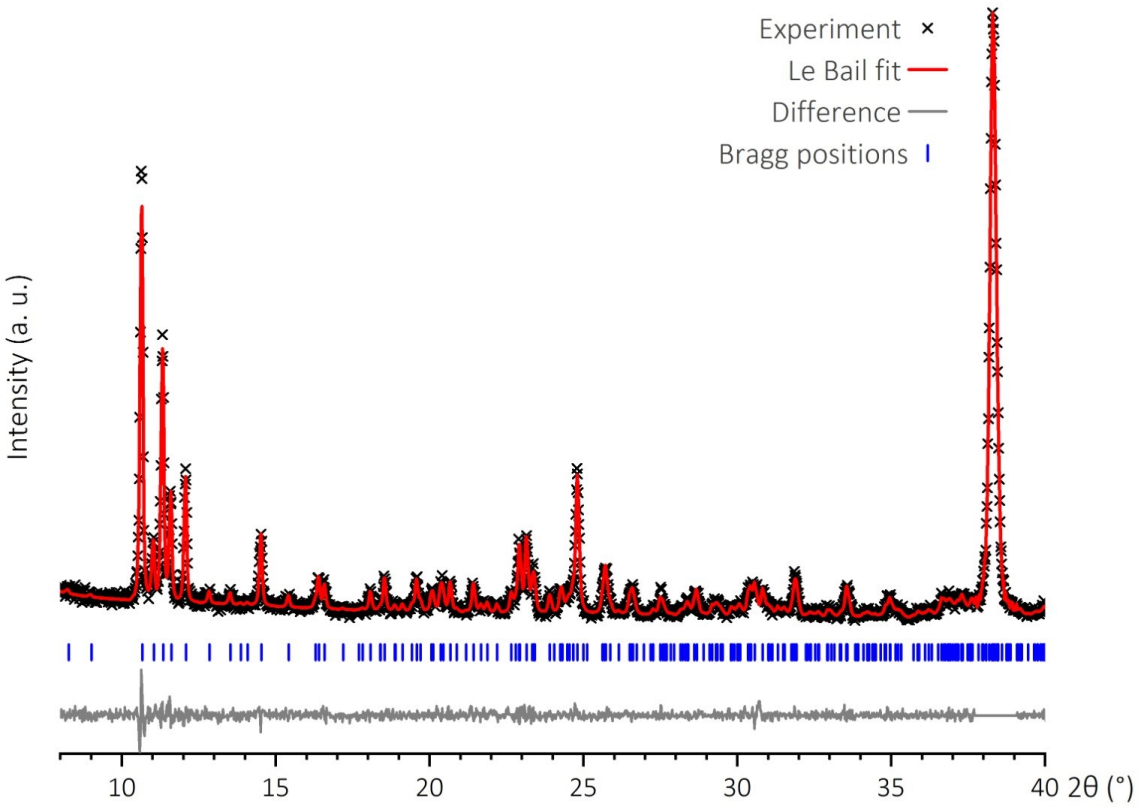


**Figure S13** Experimental powder diffraction pattern (black crosses) for complex **1** synthesized from $Fe(BF_4)_2 \cdot 6\,H_2O$, Le Bail profile matching fit with parameters reported in **Table S2** (red lines), with corresponding Bragg peaks' positions (blue markers), and fit residual (grey line).

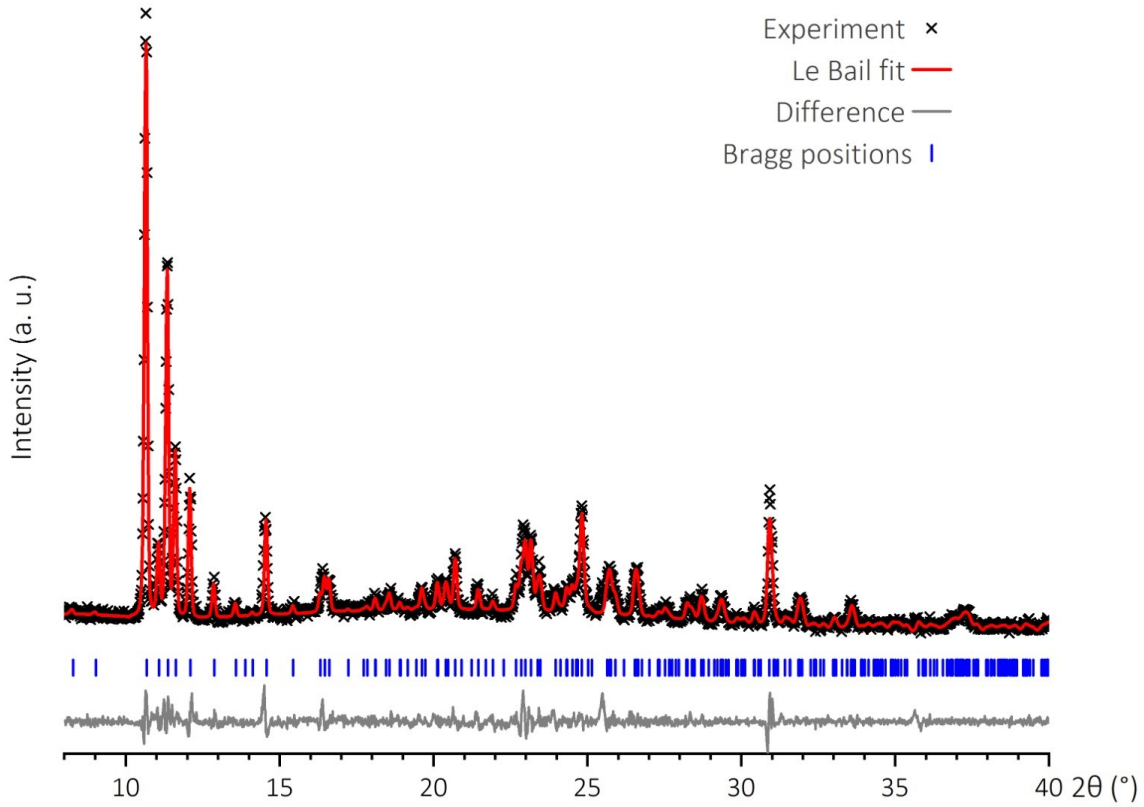


**Figure S14** Experimental powder diffraction pattern (black crosses) for complex **1** synthesized from $Fe(ClO_4)_2 \cdot x\ H_2O$, Le Bail profile matching fit with parameters reported in **Table S2** (red lines), with corresponding Bragg peaks' positions (blue markers), and fit residual (grey line).

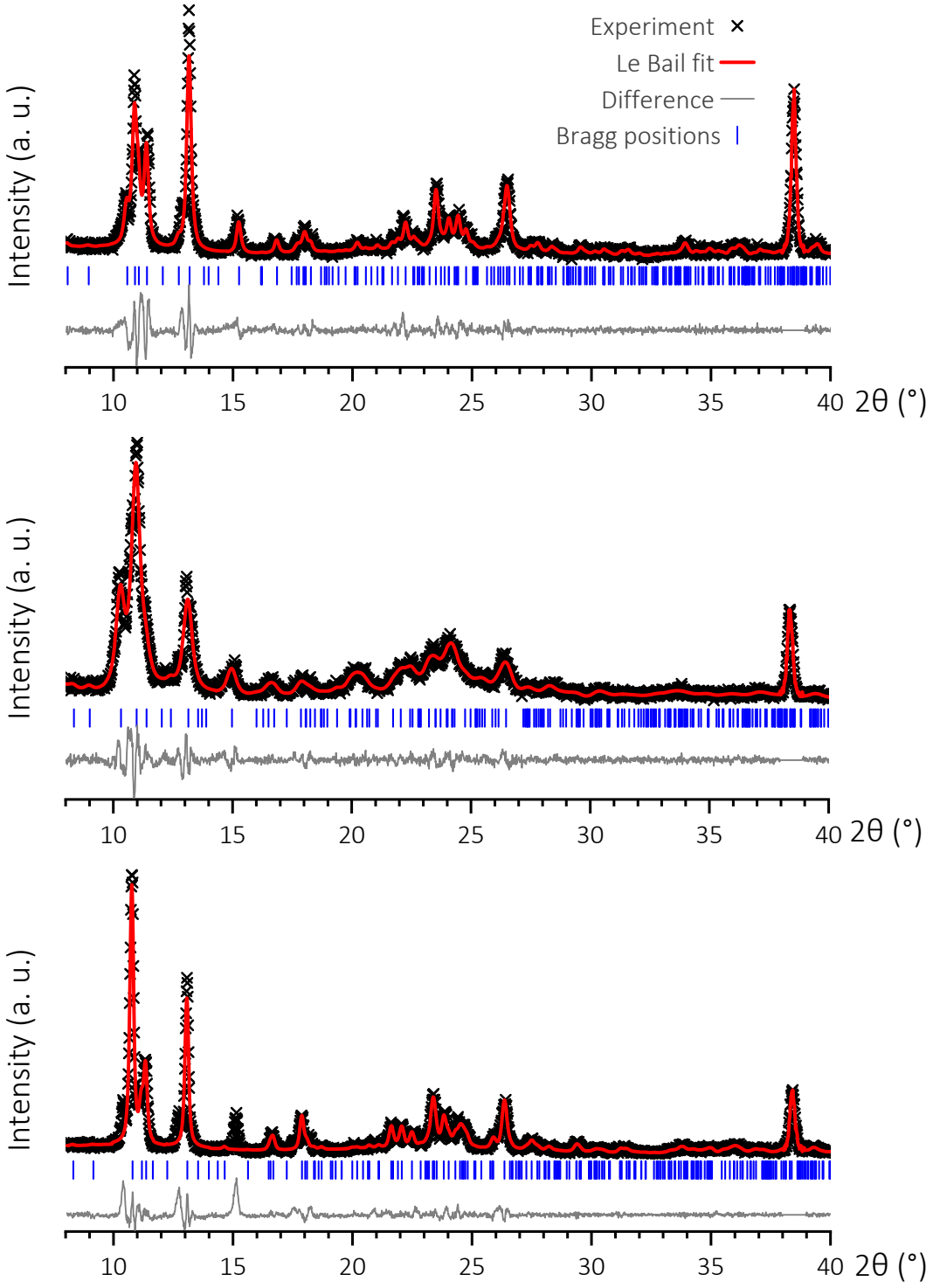


**Figure S15** Experimental powder diffraction patterns (black crosses) of the three fractions collected upon sublimation of complex **1**, Le Bail profile matching fits with parameters reported in **Table S2** (red lines), with corresponding Bragg peaks' positions (blue markers), and fit residuals (grey line).

**Table S2**: Unit cells resulting from the Le Bail profile matching fits performed on the powder diffraction patterns measured on the three batches of complex **1** and the three fractions collected upon sublimation.

| | Iron precursor | | | Sublimed | | |
|---|---|---|---|---|---|---|
| | $FeSO_4$ | $Fe(BF_4)_2$ | $Fe(ClO_4)_2$ | F1 | F2 | F3 |
| *a* (Å) | 9.897(1) | 9.891(8) | 9.870(1) | 9.959(5) | 9.957(6) | 9.7456(6) |
| *b* (Å) | 10.751(3) | 10.7462(10) | 10.736(1) | 10.997(4) | 10.792(6) | 10.698(7) |
| *c* (Å) | 12.222(2) | 12.248(1) | 12.215(1) | 12.374(5) | 12.028(7) | 12.139(9) |
| α (°) | 92.98(1) | 93.044(5) | 93.107(6) | 91.94(3) | 97.89(4) | 92.37(4) |
| β (°) | 95.04(2) | 94.946(6) | 94.777(8) | 95.68(2) | 96.03(4) | 95.01(6) |
| γ (°) | 95.526(8) | 95.528(7) | 95.511(9) | 96.08(3) | 97.21(4) | 96.43(4) |
| V (Å3) | 1287.0(5) | 1288.5(2) | 1281.4(3) | 1339.6(12) | 1260.2(9) | 1251(2) |
| $wR_p$ | 11.68 | 10.64 | 11.17 | 12.87 | 10.81 | 14.80 |
| $cwR_p$ | 20.72 | 21.49 | 19.91 | 21.19 | 13.41 | 24.58 |

**Table S3**: Single-crystal X-ray diffraction data collection and refinement information for compound **1**.

| Temperature/K | 120(2) | 250(2) | 300(2) | 320(2) | 340(2) | 360(2) | 380(2) |
|---|---|---|---|---|---|---|---|
| Empirical formula , Formula weight | $C_{22}H_{28}B_2FeN_{12}$ 538.03 | | | | | | |
| Crystal system, space group | Triclinic, *P*-1 | | | | | | |
| a/Å | 9.7267(6) | 9.8079(3) | 9.8706(5) | 9.9075(6) | 9.9492(5) | 9.9836(4) | 10.0087(7) |
| b/Å | 10.5289(7) | 10.6387(3) | 10.7248(5) | 10.7822(6) | 10.8446(5) | 10.9033(5) | 10.9499(8) |
| c/Å | 12.1811(8) | 12.2147(3) | 12.2325(5) | 12.2486(6) | 12.2727(5) | 12.2973(5) | 12.3131(9) |
| α/° | 93.485(4) | 93.176(2) | 93.064(4) | 93.059(4) | 93.048(3) | 93.054(3) | 93.042(5) |
| β/° | 95.007(4) | 94.880(2) | 94.942(3) | 94.959(3) | 94.995(3) | 95.025(3) | 95.035(5) |
| γ/° | 95.425(4) | 95.584(2) | 95.509(3) | 95.424(3) | 95.353(3) | 95.275(3) | 95.212(5) |
| Volume/Å$^3$ | 1234.16(14) | 1261.27(6) | 1281.67(10) | 1295.22(12) | 1310.87(10) | 1325.28(10) | 1336.14(17) |
| Z | 2 | | | | | | |
| $\rho_{calc}$g/cm$^3$ | 1.448 | 1.417 | 1.394 | 1.380 | 1.363 | 1.348 | 1.337 |
| μ/mm$^{-1}$ | 0.650 | 0.636 | 0.626 | 0.619 | 0.612 | 0.605 | 0.600 |
| F(000) | 560.0 | | | | | | |
| Crystal size/mm$^3$ | 0.4 × 0.12 × 0.1 | | | | | | |
| 2Θ range for data collection/° | 6.474 to 55.038 | 6.424 to 55.014 | 6.5 to 54.994 | 6.224 to 55.024 | 6.358 to 55.008 | 6.178 to 55.058 | 6.998 to 55.056 |
| Index ranges | -12 ≤ h ≤ 11, -12 ≤ k ≤ 13, -15 ≤ l ≤ 15 | -12 ≤ h ≤ 12, -13 ≤ k ≤ 13, -15 ≤ l ≤ 15 | -12 ≤ h ≤ 12, -13 ≤ k ≤ 13, -15 ≤ l ≤ 15 | -12 ≤ h ≤ 12, -13 ≤ k ≤ 13, -15 ≤ l ≤ 15 | -12 ≤ h ≤ 12, -13 ≤ k ≤ 14, -15 ≤ l ≤ 15 | -12 ≤ h ≤ 12, -14 ≤ k ≤ 14, -15 ≤ l ≤ 15 | -12 ≤ h ≤ 12, -13 ≤ k ≤ 14, -16 ≤ l ≤ 15 |
| Reflections collected | 9014 | 10381 | 10923 | 11033 | 11120 | 11250 | 10187 |
| Independent reflections | 5621 [$R_{int}$ = 0.0209 $R_{sigma}$ = 0.0429] | 5761 [$R_{int}$ = 0.0127 $R_{sigma}$ = 0.0200] | 5829 [$R_{int}$ = 0.0179 $R_{sigma}$ = 0.0298] | 5885 [$R_{int}$ = 0.0185 $R_{sigma}$ = 0.0306] | 5952 [$R_{int}$ = 0.0151 $R_{sigma}$ = 0.0261] | 6022 [$R_{int}$ = 0.0160 $R_{sigma}$ = 0.0270] | 6028 [$R_{int}$ = 0.0193 $R_{sigma}$ = 0.0356] |
| Data/restraints/parameters | 5621/0/349 | 5761/0/349 | 5829/0/341 | 5885/0/349 | 5952/0/349 | 6022/0/349 | 6028/0/349 |
| Goodness-of-fit on F$^2$ | 1.038 | 1.057 | 1.025 | 1.031 | 1.035 | 1.044 | 1.019 |
| Final R indexes [I>=2σ (I)] | $R_1$ = 0.0388 $wR_2$ = 0.0927 | $R_1$ = 0.0380 $wR_2$ = 0.0999 | $R_1$ = 0.0395 $wR_2$ = 0.1044 | $R_1$ = 0.0405 $wR_2$ = 0.1048 | $R_1$ = 0.0416 $wR_2$ = 0.1084 | $R_1$ = 0.0432 $wR_2$ = 0.1094 | $R_1$ = 0.0447 $wR_2$ = 0.1151 |
| Final R indexes [all data] | $R_1$ = 0.0533 $wR_2$ = 0.0999 | $R_1$ = 0.0460 $wR_2$ = 0.1072 | $R_1$ = 0.0560 $wR_2$ = 0.1171 | $R_1$ = 0.0609 $wR_2$ = 0.1198 | $R_1$ = 0.0600 $wR_2$ = 0.1248 | $R_1$ = 0.0633 $wR_2$ = 0.1260 | $R_1$ = 0.0749 $wR_2$ = 0.1378 |
| Largest diff. peak/hole / e$^-$Å$^{-3}$ | 0.31/-0.48 | 0.38/-0.42 | 0.40/-0.32 | 0.42/-0.32 | 0.37/-0.33 | 0.28/-0.27 | 0.34/-0.31 |

| Temperature/K | 350(2) | 330(2) | 300(2) |
|---|---|---|---|
| Empirical formula | $C_{22}H_{28}B_2FeN_{12}$ | | |
| Formula weight | 538.03 | | |

| Crystal system, space group | Triclinic, *P*-1 | | |
|---|---|---|---|
| a/Å | 9.9676(7) | 9.9257(7) | 9.8669(4) |
| b/Å | 10.8692(8) | 10.8110(8) | 10.7177(4) |
| c/Å | 12.2898(8) | 12.2594(9) | 12.2314(5) |
| α/° | 92.987(5) | 93.045(5) | 93.061(3) |
| β/° | 95.018(5) | 94.963(5) | 94.938(3) |
| γ/° | 95.350(5) | 95.384(5) | 95.503(2) |
| Volume/Å$^3$ | 1318.15(16) | 1302.31(16) | 1280.25(9) |
| Z | 2 | | |
| $\rho_{calc}$g/cm$^3$ | 1.356 | 1.372 | 1.396 |
| μ/mm$^{-1}$ | 0.608 | 0.616 | 0.626 |
| F(000) | 560.0 | | |
| Crystal size/mm$^3$ | 0.4 × 0.12 × 0.1 | | |
| 2Θ range for data collection/° | 7.036 to 54.846 | 7.066 to 54.97 | 6.502 to 54.98 |
| Index ranges | -12 ≤ h ≤ 12, -13 ≤ k ≤ 14, -15 ≤ l ≤ 15 | -12 ≤ h ≤ 12, -13 ≤ k ≤ 14, -15 ≤ l ≤ 15 | -12 ≤ h ≤ 12, -13 ≤ k ≤ 13, -15 ≤ l ≤ 15 |
| Reflections collected | 9919 | 9959 | 10936 |
| Independent reflections | 5893 [$R_{int}$ = 0.0190 $R_{sigma}$ = 0.0365] | 5887 [$R_{int}$ = 0.0206 $R_{sigma}$ = 0.0408] | 5815 [$R_{int}$ = 0.0144 $R_{sigma}$ = 0.0229] |
| Data/restraints/parameters | 5893/0/349 | 5887/0/349 | 5815/0/349 |
| Goodness-of-fit on F$^2$ | 1.033 | 1.010 | 1.053 |
| Final R indexes [I>=2σ (I)] | $R_1$ = 0.0438 $wR_2$ = 0.1108 | $R_1$ = 0.0432 $wR_2$ = 0.1085 | $R_1$ = 0.0389 $wR_2$ = 0.1006 |
| Final R indexes [all data] | $R_1$ = 0.0665 $wR_2$ = 0.1294 | $R_1$ = 0.0690 $wR_2$ = 0.1255 | $R_1$ = 0.0506 $wR_2$ = 0.1124 |
| Largest diff. peak/hole / e Å$^{-3}$ | 0.35/-0.33 | 0.41/-0.31 | 0.35/-0.40 |

A close but not identical structure was observed previously when crystals were obtained starting from an impure ligand (synthesized following path A). The crystals showed the same triclinic *P*-1 spacegroup, but with a different unit cell: *a*=9.72, b=10.79 , c=13.74 Å, α=81.98, β=80.00, γ=66.68°. The crystals were poorly diffracting, with no peaks observed beyond 0.9Å, which did not allow for a precise structural determination. Nevertheless 2 half-complexes can be observed in the unit cell, with iron atoms lying on special positions. On at least one of the complexes the ligand seemed to present overlapping pyrazole and dimethylpyrazole groups, suggesting a mixture of ligands in the structure.

**Table S4**: distortion parameters vs. temperature calculated with the OCTADIST software[3] for compound **1**, and compounds [Fe(HB(pz)$_3$)$_2$] (CCDC refcodes HPZBFE03 and HPZBFE05), and Fe(HB(dmpz)$_3$)$_2$] (CCDC refcodes HMPBFE03 and HPZBFE02).

| T (K) | <Fe1-N> (Å) | <Fe2-N> (Å) | Fe1 ζ (Å) | Fe2 ζ (Å) | Fe1 Δ | Fe2 Δ | Fe1 Σ (°) | Fe2 Σ (°) | Fe1 Θ (°) | Fe2 Θ (°) |
|---|---|---|---|---|---|---|---|---|---|---|
| Complex **1** | | | | | | | | | | |
| 120 | 1.9835 | 1.9794 | 0.09694 | 0.06209 | 8E-5 | 3.1E-5 | 16.4964 | 17.3195 | 42.6909 | 45.8761 |
| 250 | 1.9898 | 1.9851 | 0.09213 | 0.07527 | 7.1E-5 | 4.6E-5 | 16.1039 | 18.0686 | 44.2516 | 48.2784 |
| 300 | 2.0145 | 2.0095 | 0.09399 | 0.07972 | 7.2E-5 | 4.9E-5 | 19.7621 | 20.7491 | 58.8401 | 60.6662 |
| 320 | 2.0412 | 2.037 | 0.09568 | 0.09216 | 7.2E-5 | 6.4E-5 | 24.1731 | 25.58 | 68.9892 | 73.673 |
| 340 | 2.0715 | 2.0722 | 0.09625 | 0.09162 | 7.1E-5 | 6.2E-5 | 30.7264 | 32.0136 | 83.959 | 88.4285 |
| 360 | 2.1001 | 2.1014 | 0.09534 | 0.09121 | 7.1E-5 | 6E-5 | 36.6953 | 38.0608 | 97.4035 | 102.2927 |
| 380 | 2.1186 | 2.1198 | 0.09476 | 0.08539 | 6.9E-5 | 5.3E-5 | 39.6283 | 42.0614 | 103.3821 | 110.6114 |
| 350 | 2.087 | 2.0878 | 0.09755 | 0.08554 | 7.5E-5 | 5.4E-5 | 34.1286 | 35.1874 | 91.6756 | 95.8107 |
| 330 | 2.0559 | 2.0557 | 0.09776 | 0.08383 | 7.6E-5 | 5.3E-5 | 27.9123 | 29.1192 | 77.4994 | 81.6931 |
| 300 | 2.0152 | 2.0095 | 0.09897 | 0.08635 | 8.1E-5 | 5.8E-5 | 18.909 | 20.3492 | 57.0088 | 60.9015 |
| Complex [Fe(HB(pz)$_3$)$_2$] | | | | | | | | | | |
| 180 | 1.9806 | | 0.01825 | | 0.3E-5 | | 19.1804 | | 50.3111 | |
| 420 | 2.0978 | | 0.02966 | | 1.1E-5 | | 44.5011 | | 117.2707 | |
| Complex [Fe(HB(dmpz)$_3$)$_2$] | | | | | | | | | | |
| 100 | 1.9948 | | 0.01576 | | 0.2E-5 | | 2.5368 | | 7.7519 | |
| RT | 2.1782 | | 0.07394 | | 3.7E-5 | | 39.8897 | | 92.8518 | |

ζ and Δ are radial distorsion parameters: $\zeta = \sum_{i=1}^{6} |d_i - d_{mean}|$ and $\Delta = \frac{1}{6}\sum_{i=1}^{6}\left(\frac{d_i - d_{mean}}{d_{mean}}\right)^2$, where $d_i$ are the individual Fe-N bond lengths and $d_{mean}$ their average.

Σ is an angular distorsion parameter: $\Sigma = \sum_{i=1}^{12} |90 - \varphi_i|$, where $\varphi_i$ are the 12 N-Fe-N angles.

[3] R. Ketkaew, Y. Tantirungrotechai, P. Harding, G. Chastanet, P. Guionneau, M. Marchivie, D. J. Harding *Dalton Trans.*, **2021**, *50*, 1086.

$\Theta$ is a torsonial distorsion parameter: $\Theta = \sum_{i=1}^{24} |60 - \theta_i|$, where $\theta_i$ are the 24 angles between two vectors of opposed twisting faces.

**Table S5**: Continuous Symmetry Measure[4,5] and Continuous Shape Measure[6] vs. temperature calculated with the online *CoSyM* tool for compound **1**, and compounds [Fe(HB(pz)$_3$)$_2$] (CCDC refcodes HPZBFE03 and HPZBFE05), and Fe(HB(dmpz)$_3$)$_2$] (CCDC refcodes HMPBFE03 and HPZBFE02). The *C*2 symmetry point group and octahedral shape were chosen for the calculations. Note that for both measures values range from 0 (perfect agreement with symmetry or shape) to 100.

| T (K) | CSM *C*2 Fe1 | CCM *C*2 Fe2 | CShM $O_h$ Fe1 | CShM $O_h$ Fe2 |
|---|---|---|---|---|
| Compound **1** | | | | |
| 120 | 0.1064 | 0.0301 | 0.043 | 0.0428 |
| 250 | 0.0824 | 0.0294 | 0.0432 | 0.0488 |
| 300 | 0.0779 | 0.0119 | 0.0674 | 0.0714 |
| 320 | 0.0852 | 0.0116 | 0.089 | 0.1004 |
| 340 | 0.0907 | 0.0473 | 0.1283 | 0.1407 |
| 360 | 0.0957 | 0.0315 | 0.1712 | 0.1865 |
| 380 | 0.1126 | 0.113 | 0.1939 | 0.2179 |
| 350 | 0.0792 | 0.0346 | 0.152 | 0.164 |
| 330 | 0.0949 | 0.0124 | 0.1103 | 0.121 |
| 300 | 0.0783 | 0.0245 | 0.0652 | 0.0716 |
| Complex [Fe(HB(pz)$_3$)$_2$] | | | | |
| 180 | 0.0136 | | 0.0505 | |
| 420 | 0.0209 | | 0.2489 | |
| Complex [Fe(HB(dmpz)$_3$)$_2$]* | | | | |
| 100 | 0.0054 | | 0.0012 | |
| RT | 0.0585 | | 0.1726 | |

* The methyl groups' hydrogen atoms had to be removed for the CSM calculation.

[4] M. Pinsky, C. Dryzun, D. Casanova, P. Alemany, D. Avnir *J. Comput. Chem.*, **2008**, *29,* 2712.
[5] G. Alon, I. Tuvi-Arad *J. Math. Chem.*, **2018**, *56*, 193.
[6] S. Alvarez *Chem. Rev.*, **2015**, *115*, 13447.

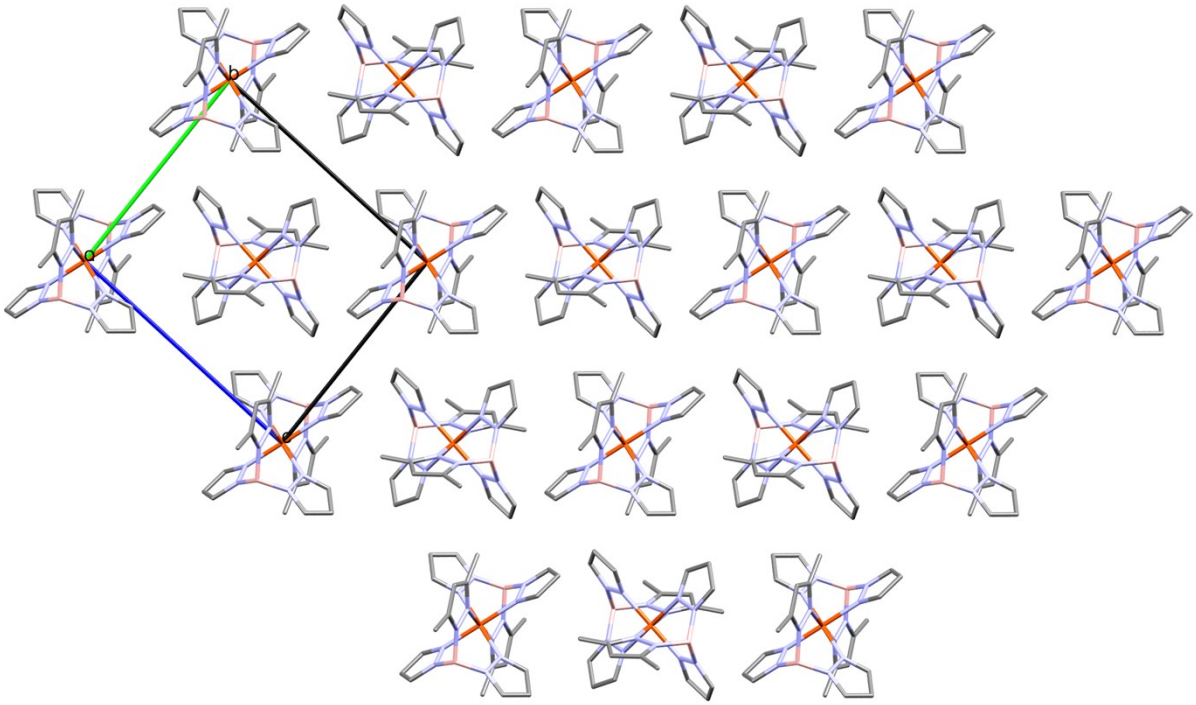

**Figure S16** View of complex **1** crystal packing, as seen along the *a* axis. Hydrogen atoms were omitted for clarity.

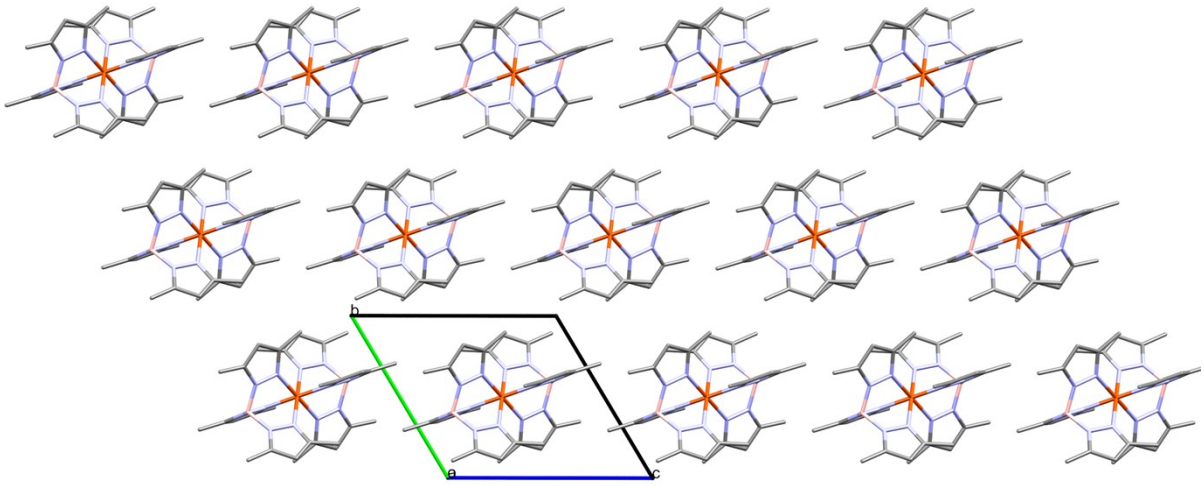


**Figure S17** View of complex [Fe(HB(dmpz)$_3$)$_2$] crystal packing at 100 K (CCSD refcode HMBPFE03), as seen along the *a* axis. Hydrogen atoms were omitted for clarity.

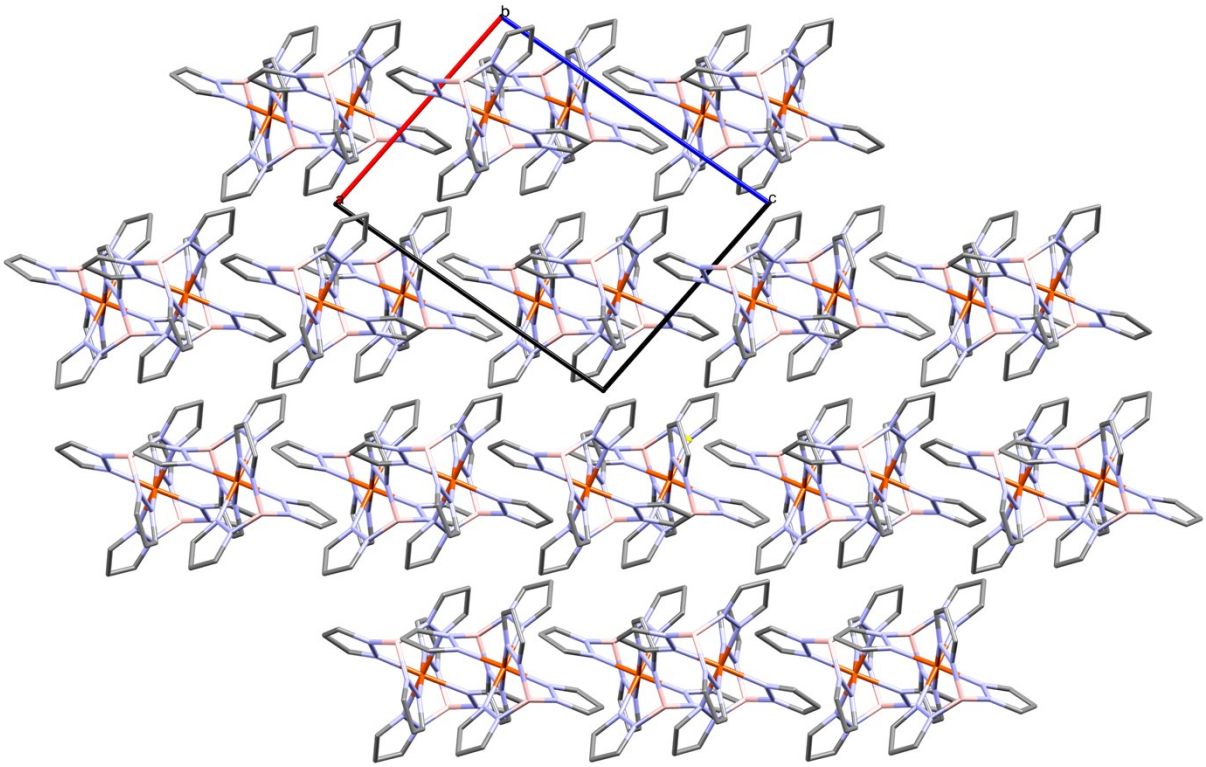


**Figure S18** View of complex $[Fe(HB(pz)_3)_2]$ crystal packing at 180 K (CCSD refcode HPZBFE03), as seen along the *b* axis. Hydrogen atoms were omitted for clarity.

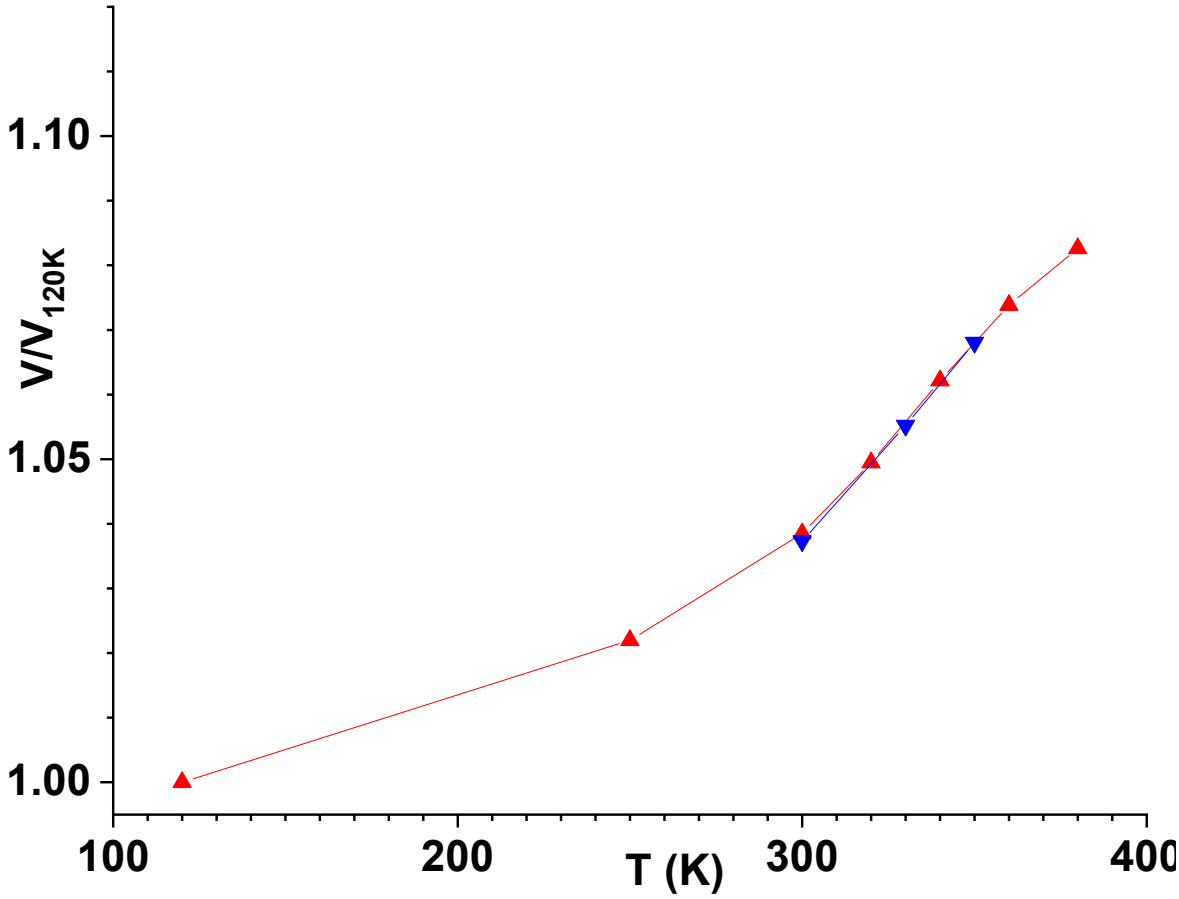


**Figure S19** Evolution with temperature of the unit cell volume for complex **1**, normalized by the value measured at 120 K.

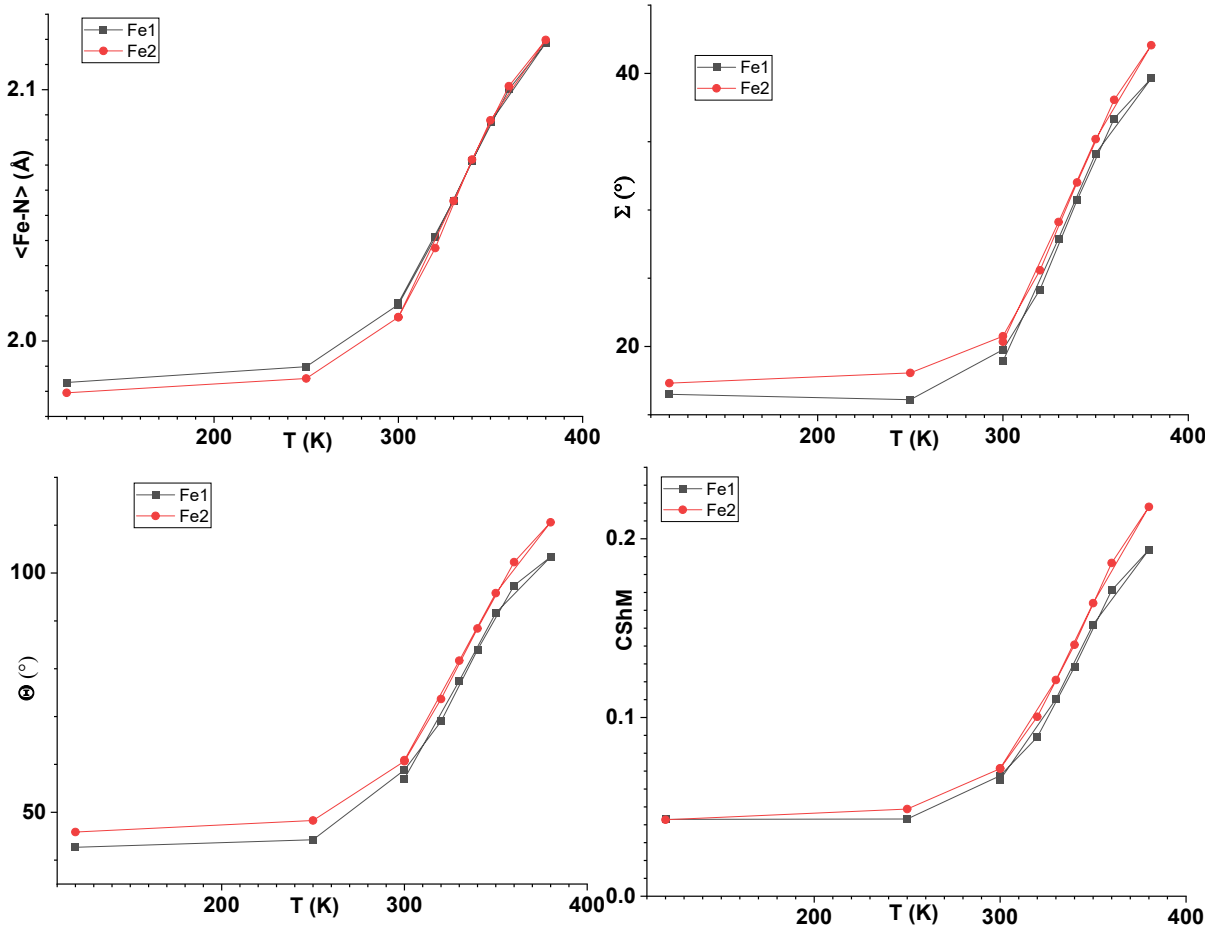


**Figure S20** Evolution with temperature for the structure of complex **1** of the average Fe-N bond length (top left), of angular and torsional distorsion parameters Σ and Θ (top right and bottom left), and of the Continuous Shape Measure respective to octahedral symmetry (bottom right).

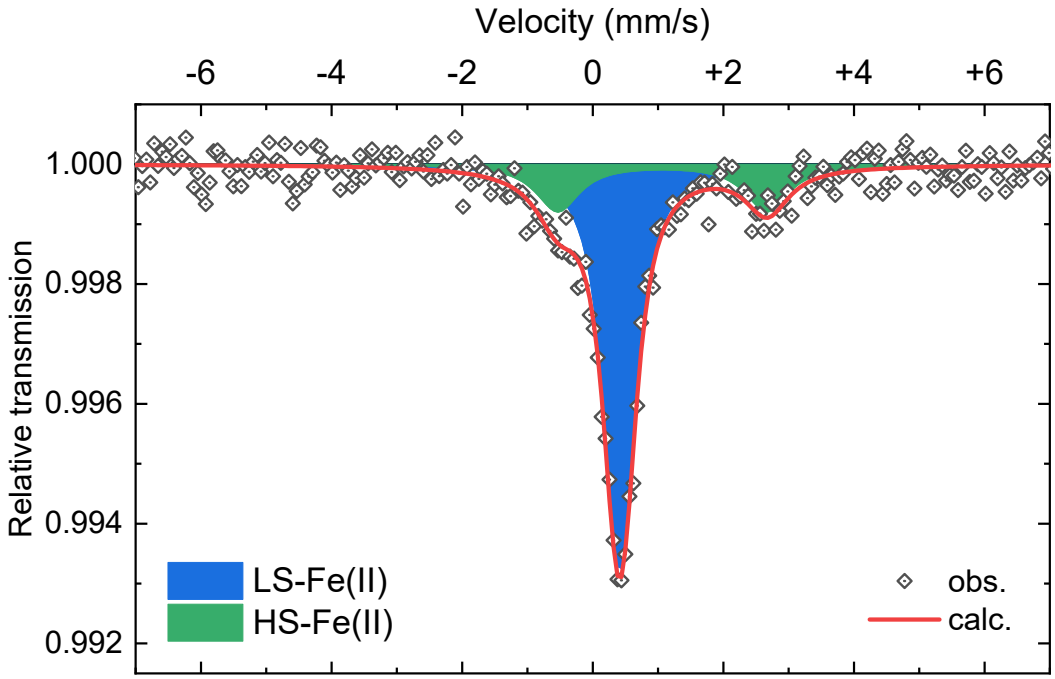


**Figure S21** Mössbauer spectrum of complex **1** at 295 K (black diamonds), with the LS (in blue) and HS (in green) components, and the total resulting fit (red curve). Isotopic shifts $\delta$, quadrupolar splittings $\Delta$, linewidths $\Gamma$ and relative area are reported here below.

| | $\delta$ (mm/s) | $\Delta$ (mm/s) | $\Gamma$ (mm/s) | Relative area (%) |
|---|---|---|---|---|
| LS-Fe(II) | 0.41(2) | 0.15(5) | 0.53(4) | 75(5) |
| HS-Fe(II) | 1.07(4) | 3.20(9) | 0.82(9) | 25(5) |

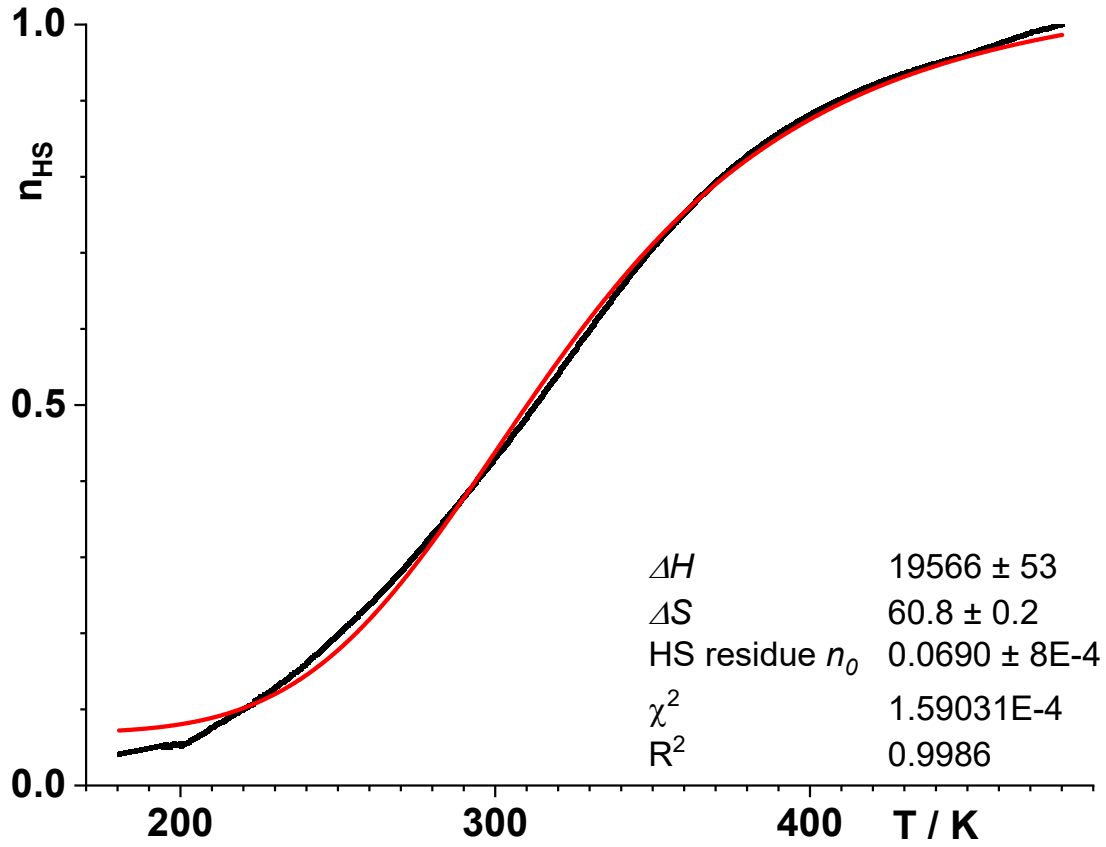


**Figure S22** HS fraction $n_{HS}$ variation with temperature and fit with a simple two-state Boltzmann dependence $n_{HS} = 1/\left(1 + exp\left(\Delta H/RT - \Delta S/R\right)\right) + n_0$, $n_0$ being a low-temperature HS residue. The $n_{HS}$ curve was obtained by averaging the curves represented in Figure 2 in the main text.

## Scanning tunnel Microscopy

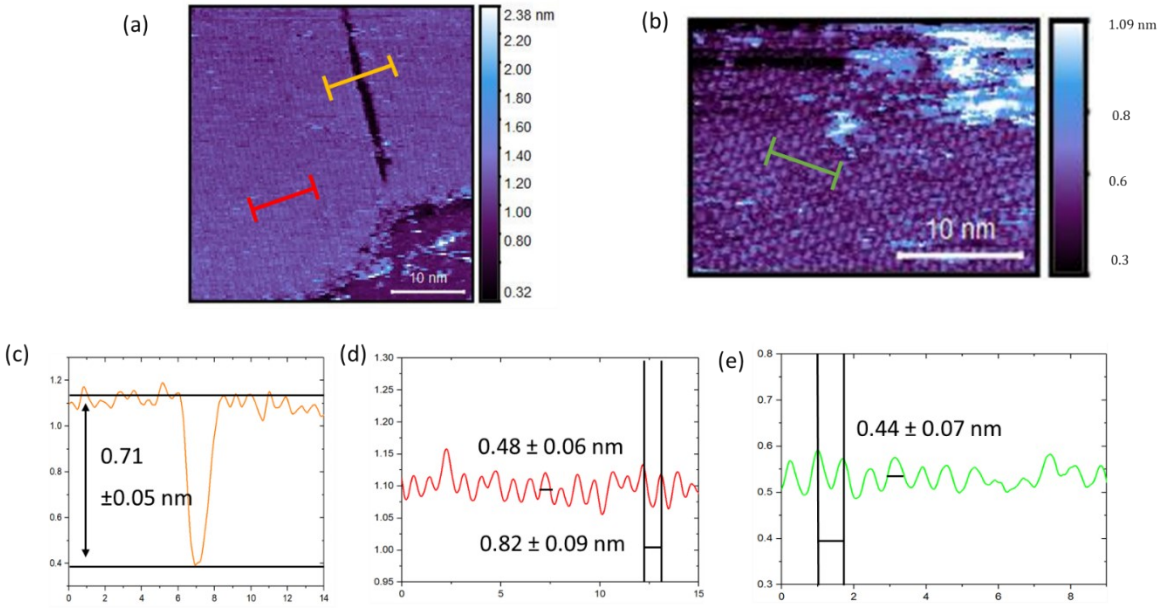


**Figure S23** STM images performed at constant current in UHV. STM image on (a) **1**/Au(111) and (b) on **1**/HOPG. (c) and (d) are the profile relative to image (a) and (e) to image (b).

**X-ray Photoelectron Spectroscopy**

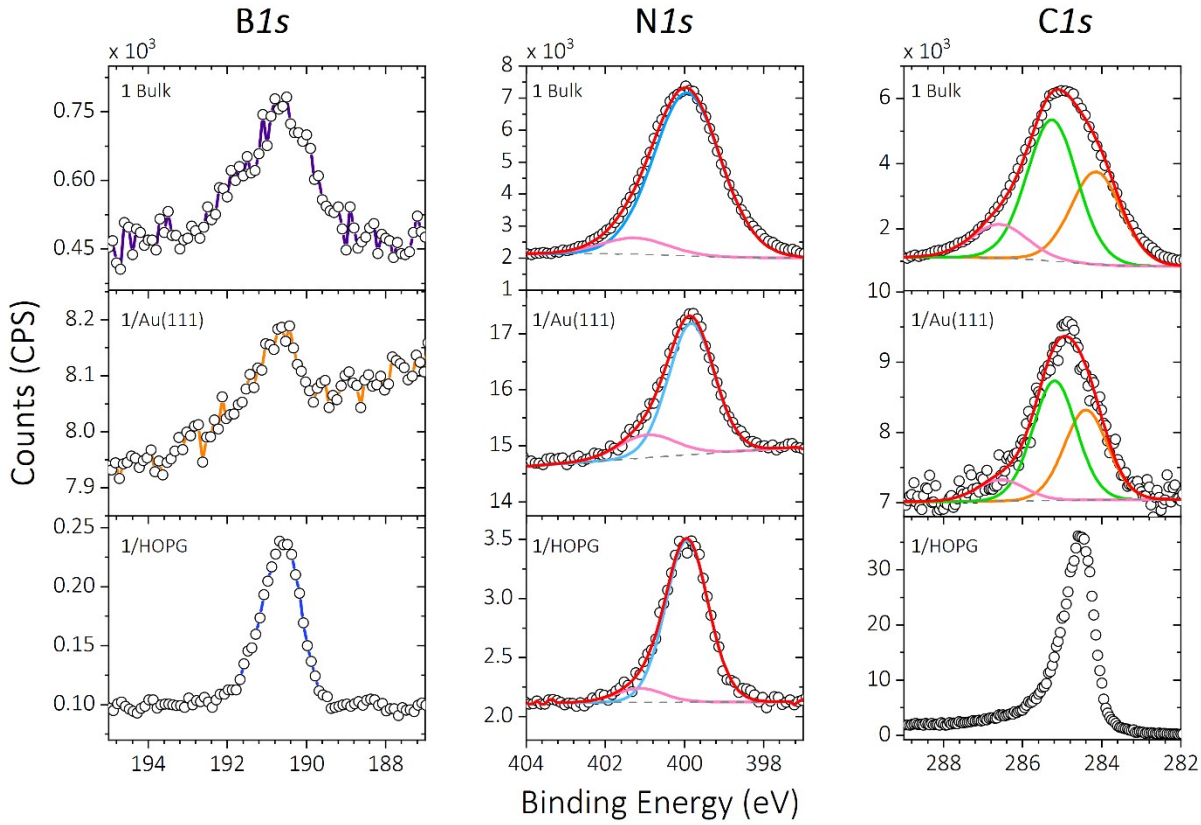


**Figure S24** XPS spectra in the regions of interest related to B*1s* (left), N*1s* (centre), and C*1s* (right). Black spheres indicate experimental data and red lines the fitting result sum of all the Voigt components (see method section). The $sp^2$ and $sp^3$ carbon component of C*1s* is represented in orange, the C-N component in green, with its shake-up in pink. For N*1s*, the N-B and N-Fe component is represented in blue, with its shake-up in pink.

**Table S6**: Relationship between deposition time and Au/C ratio (at 300K)..

| Deposition time (min) | Au/C |
|---|---|
| 150 | 3.21 |
| 175 | 3.02 |
| 45 | 3.00 |
| 30 | 4.04 |

**Table S7**: Stoichiometry evaluated from XPS spectra and related to 1/Au(111), microcrystalline powder and 1/HOPG.

| | **1**/Au(111) | **1 Bulk** | **Theoretical** | **1/HOPG** | **Theoretical no C** |
|---|---|---|---|---|---|
| **C*1s*** | 60.9% | 61.5% | 59.5% | // | // |
| **N*1s*** | 31.8% | 31.0% | 32.4% | 79.6% | 80.0% |
| **Fe*2p*** | 2.9% | 2.9% | 2.7% | 6.6% | 6.7% |
| **B*1s*** | 4.4% | 4.6% | 5.4% | 13.8% | 13.3% |

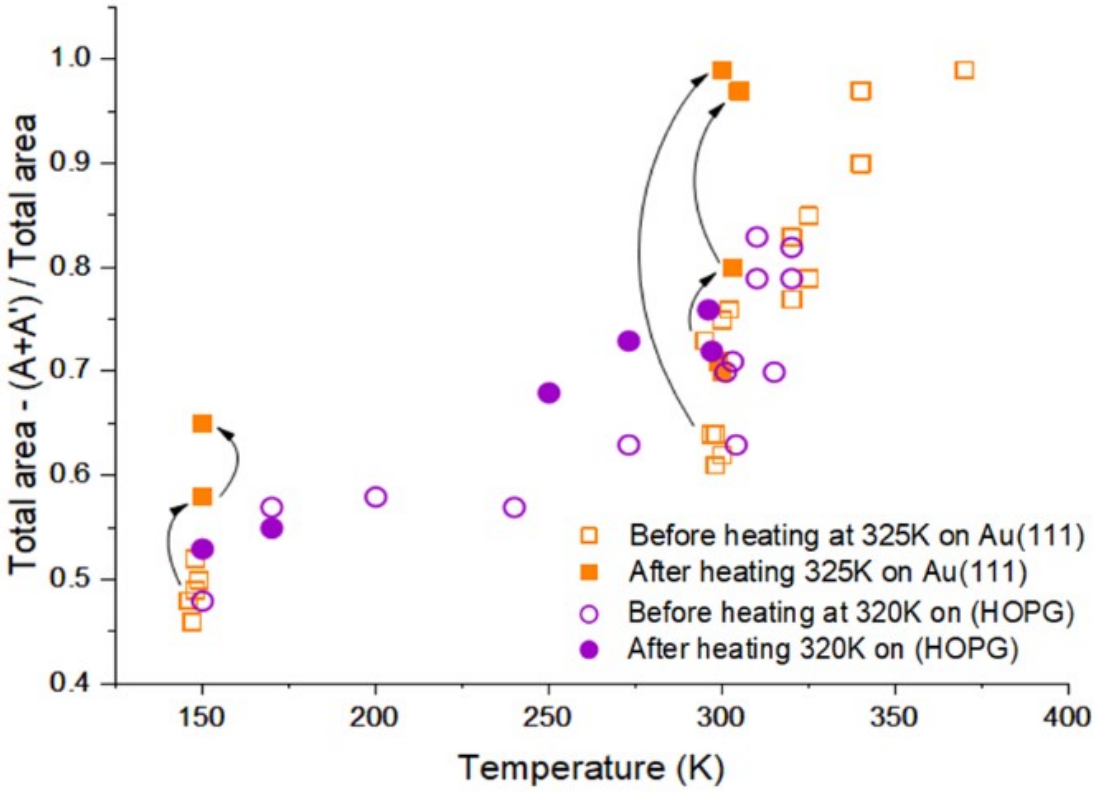


**Figure S25** Difference of the A and A' components to the total Fe*2p* area, normalized to the total area of the Fe*2p* fit as a function of the temperature. The arrows are guide to the eyes to highlights the effect of the heating on the switchability of **1** on Au(111).

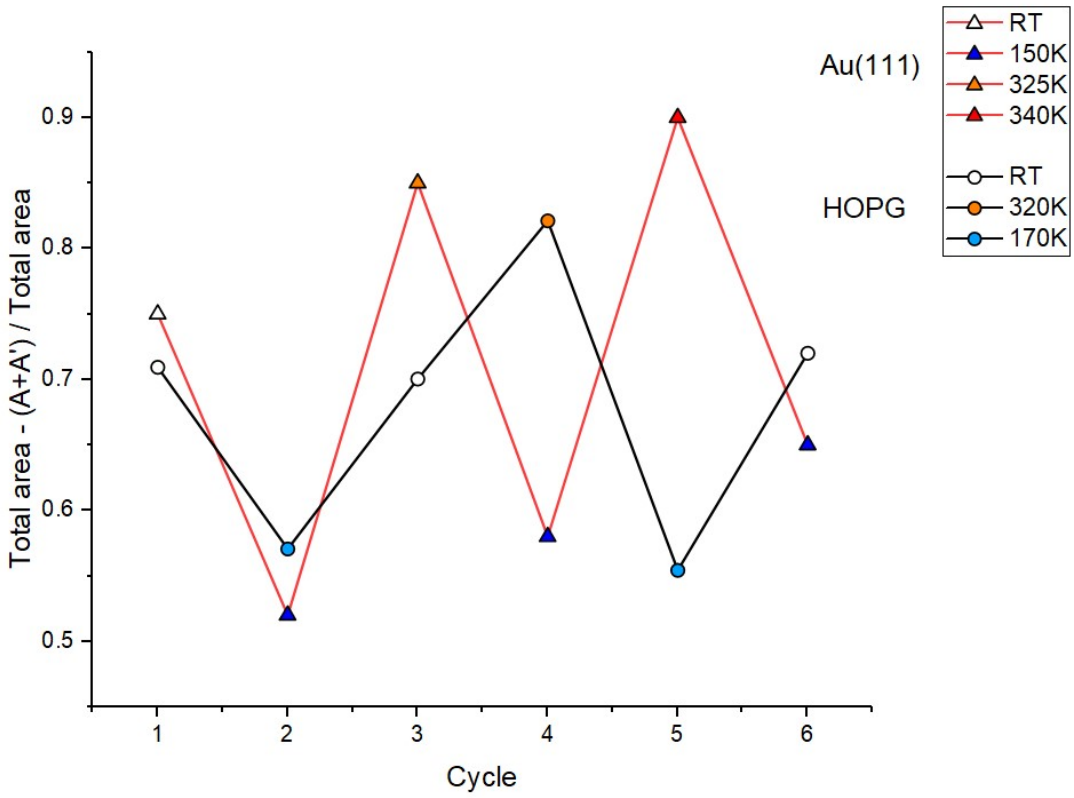


**Figure S26** Difference of the A and A' components to the total Fe*2p* area, normalized to the total area of the Fe*2p* fit as a function of the successive steps. Comparison of the effect of heating on the reversibility of **1** on Au(111) and on HOPG.

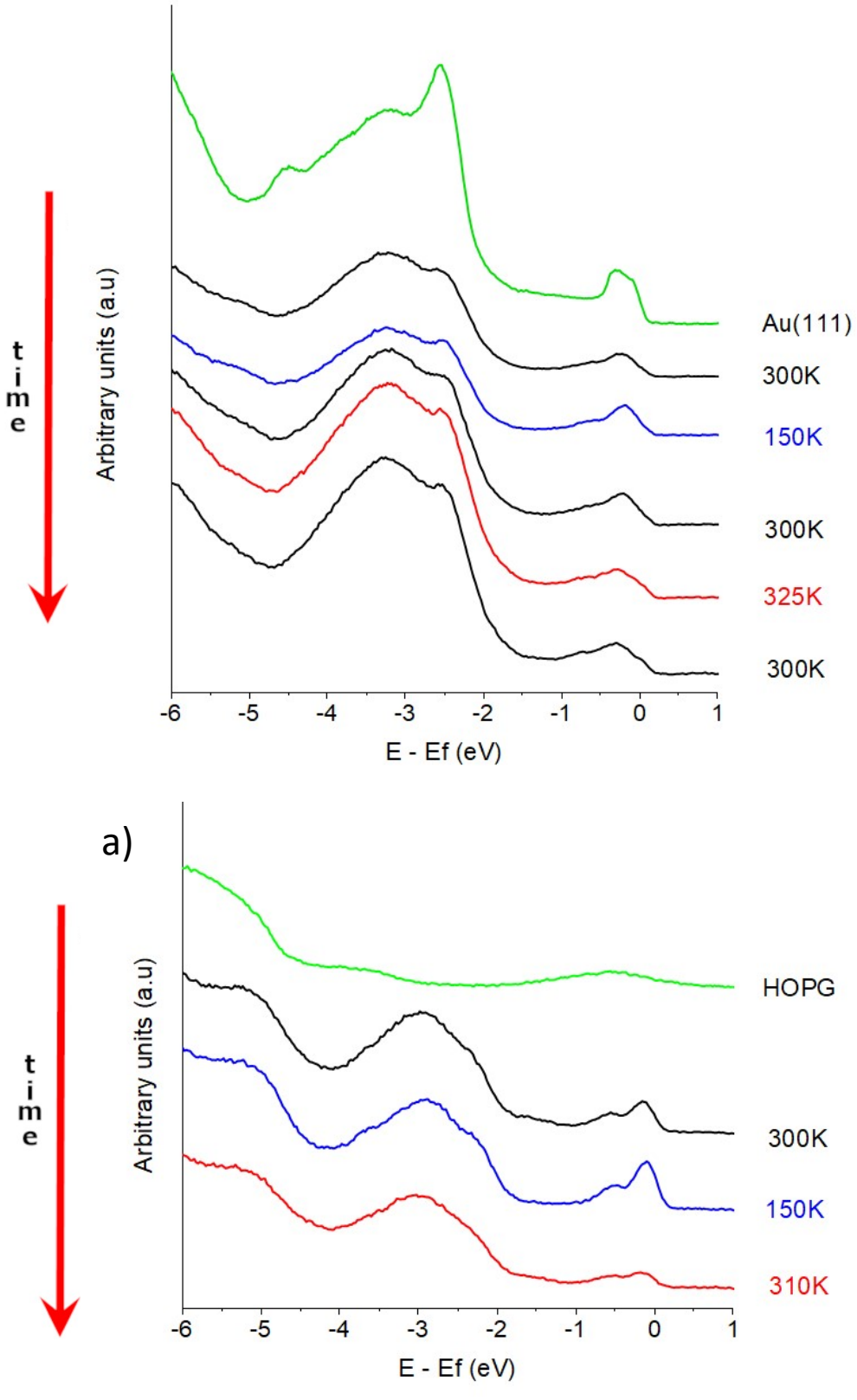


**Figure S27** UPS spectra (HeII, 40.4 eV) performed on (a) **1**/Au(111) and (b) on **1**/HOPG as a function of temperature.

## X-ray Absorption Spectroscopy

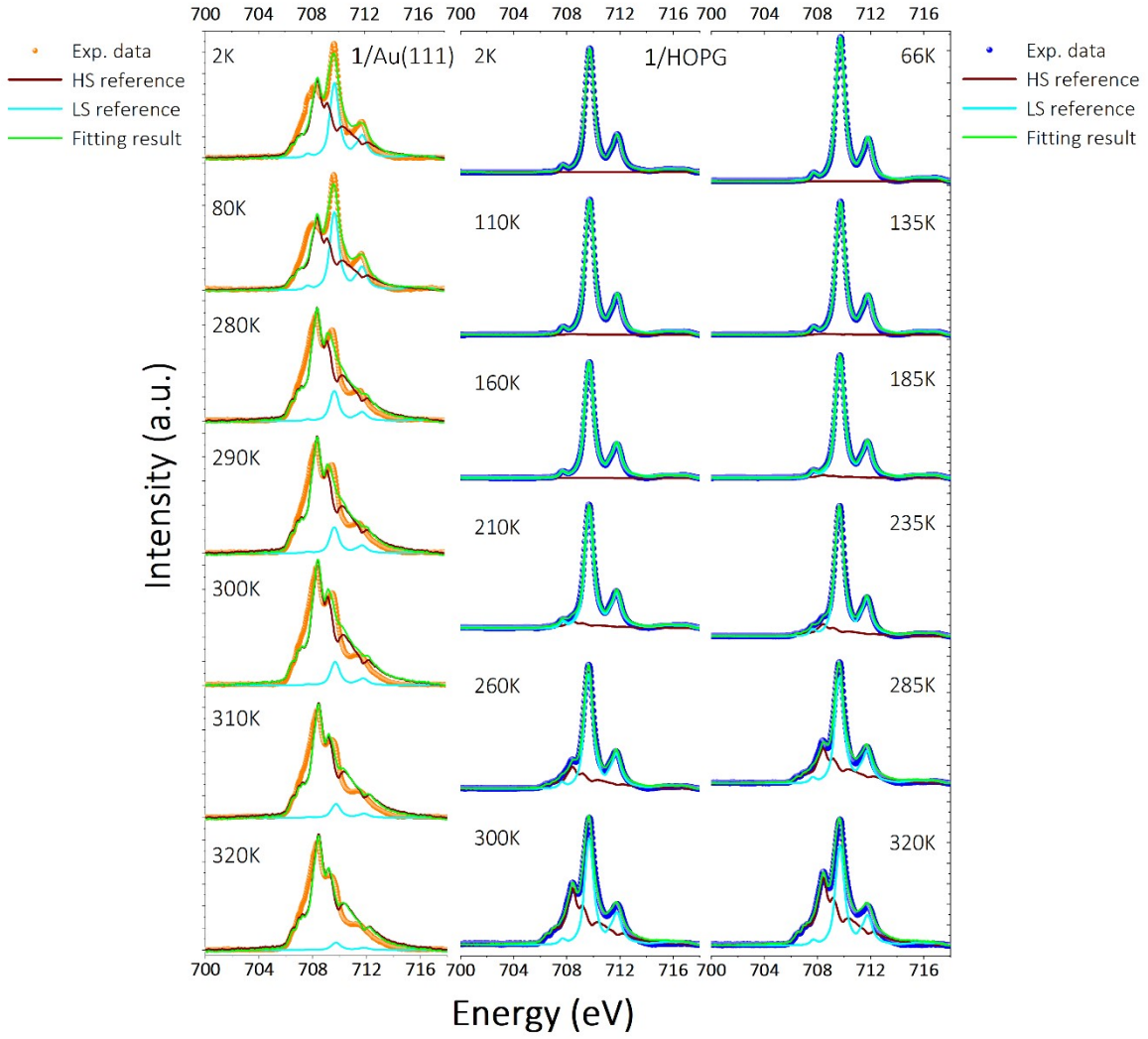


**Figure S28** Complete temperatures series of all the fitted Fe $L_3$ edge spectra for nanostructured molecules of complex **1** on Au(111) (left) and on HOPG (right).

**Table S8**: Iron $L_3$ features positions and branching ratio at the lowest and highest experimental temperatures.

| | $L_3$ features positions (eV) | | Branching ratio | |
|---|---|---|---|---|
| Sample | Lowest temperature | Highest temperature | Lowest temperature | Highest temperature |
| 0.7 ML Au(111) | 708.2; 709.7; 711.8 | 708.4; 709.4; 711.1 | 0.68 (2 K) | 0.72 (320 K) |
| 0.7 ML HOPG | 709.7; 711.8 | 708.4; 709.6; 711.6 | 0.60 (100 K) | 0.72 (320 K) |

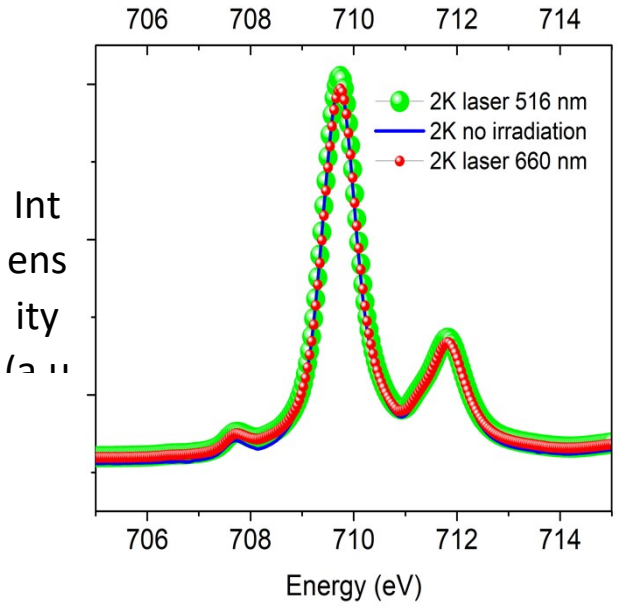


**Figure S29** 0.7 ML thick film on HOPG XAS spectra at 2K without irradiation (blue line), with irradiation at 516 nm (green spheres) and with irradiation at 660 nm (red spheres). No LIESST effect has been detected: the irradiated spectrum results identical to the spectrum recorded in the dark.

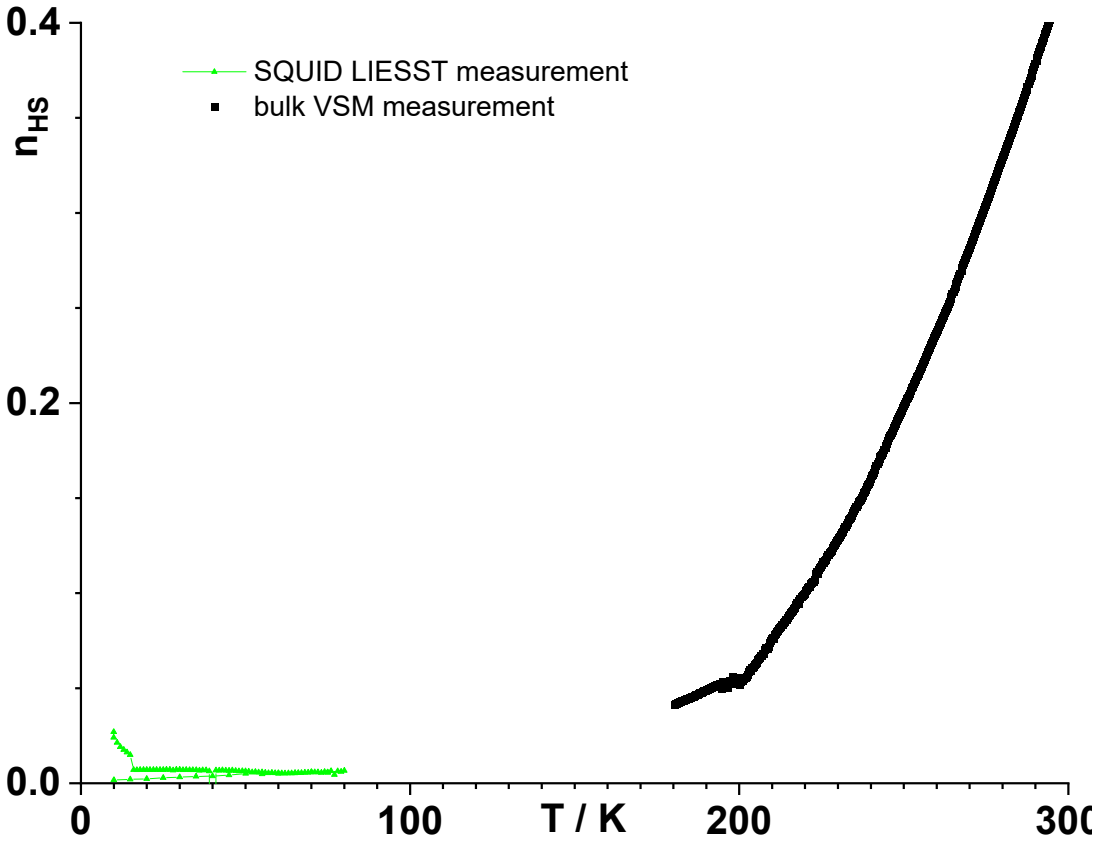


**Figure S30** Photomagnetic measurement on the bulk complex with irradiation at 532 nm (green triangles) compared to the VSM bulk measurement (black squares).